Journal of Geophysical Research: Oceans

RESEARCH ARTICLE
10.1029/2017JC013540

Subseasonal Coastal-Trapped Wave Propagations in the Southeastern Pacific and Atlantic Oceans: 2. Wave Characteristics and Connection With the Equatorial Variability

Serena Illig[1,2], Marie-Lou Bachèlery[2,3], and Emeline Cadier[2]

[1]Laboratoire d'Etudes en Géophysique et Océanographie Spatiale (LEGOS), CNRS/IRD/UPS/CNES, Toulouse, France, [2]Department of Oceanography, MARE Institute, LMI ICEMASA, University of Cape Town, Cape Town, South Africa, [3]Nansen-Tutu Centre, Marine Research Institute, Department of Oceanography, University of Cape Town, Cape Town, South Africa

This article is a companion to Illig et al. [2018], https://doi.org/10.1029/2017JC013539

Key Points:
- We observe a 15° difference in the maximum latitude at which subseasonal equatorial dynamics is detected in Southeast Pacific and Atlantic
- Different dominant CTW modes in the two ecosystems are driven by distinctive vertical structure variability in eastern equatorial regions
- Dissipation of the remotely forced CTW mode and coastal winds explain the early fading of the equatorial connection in Southeast Atlantic

Correspondence to:
S. Illig,
serena.illig@ird.fr

Citation:
Illig, S., Bachèlery, M.-L., & Cadier, E. (2018). Subseasonal coastal-trapped wave propagations in the southeastern Pacific and Atlantic Oceans: 2. Wave characteristics and connection with the equatorial variability. *Journal of Geophysical Research: Oceans*, *123*, 3942–3961. https://doi.org/10.1029/2017JC013540

Received 9 OCT 2017
Accepted 20 APR 2018
Accepted article online 3 MAY 2018
Published online 8 JUN 2018

Abstract The objective of this study is to compare the characteristics of the oceanic teleconnection with the linear equatorial dynamics of two upwelling systems along the southwestern South American and African continents at subseasonal time scales (<120 days). Altimetric data analysis shows that the coastal variability remains coherent with the equatorial signal until 27°S in the southeastern Pacific (SEP), while in the southeastern Atlantic (SEA) it fades out south of 12°S. To explain this striking difference, our methodology is based on the experimentation with twin regional model configurations of the SEP and SEA Oceans. The estimation of free Coastal-Trapped Waves (CTWs) modal structures and associated contribution to coastal variability allows inferring and comparing the characteristics of each CTW mode in the two systems; namely, their forcings, amplitude, dissipation rate, and scattering. Results show that the Pacific subseasonal equatorial forcing is only 20% larger than in the Atlantic, but important differences in the relative contribution of each baroclinic mode are reported. The first baroclinic mode dominates the eastern equatorial Pacific variability, while in the eastern equatorial Atlantic, the second mode is the most energetic. This leads to a drastic increase in the dissipation and scattering of the remotely forced CTW in the SEA sector, compared to the coastal SEP. Concomitantly, south of 15°S, the subseasonal coastal wind stress forcing is substantially more energetic in the SEA and participates in breaking the link between the equatorial forcing and the coastal variability. Our results are consistent with the solutions of a simple multimode CTW model.

Plain Language Summary The Humboldt and the Benguela upwelling systems are connected to the equatorial variability. Part of the incoming eastward equatorial wave energy is transmitted southward along the South American and African coasts as Coastal-Trapped Waves, where they imprint on the ecosystem variability. At subseasonal time scales (<120 days), altimetry reveals that the coastal variability remains coherent with the equatorial signal until 27°S in the southeastern Pacific, while in the Atlantic counterpart it fades out south of 12°S. To explain this striking difference, we compare the characteristics of coastal waves between the two systems: their forcing at the equator, their dissipation and scattering along their propagation, and the energization by the coastal wind stress. We use a variety of ocean models of different complexity ranging from regional general circulation models to simple linear coastal models. Results show that the difference between the two systems regarding the connection with the equatorial variability can be attributed to the distinct characteristics of their equatorial forcing. The latter favors fast and weakly dissipative coastal wave in the Humboldt. Off southwestern Africa, the equatorially-forced coastal-trapped waves dissipate at ~13°S and the subseasonal coastal wind stress forcing which is energetic south of 15°S, participates in breaking the link between the equatorial and coastal variabilities.

1. Introduction

Along the coasts of Peru/Chile and Angola/Namibia, the westward-moving surface waters, driven by the prevailing equatorward alongshore winds (Bakun & Nelson, 1991; Tomczak & Godfrey, 1994), allow cold and nutrient-rich water to rise up from the subsurface forming the two major Eastern Boundary Upwelling Systems (EBUS) of the Southern Hemisphere: the Humboldt and the Benguela upwelling systems. Hence, the

coastal southeastern Pacific (SEP) and southeastern Atlantic (SEA) Oceans' marine ecosystems are among the most productive and most exploited in the world (Carr, 2002; Carr & Kearns, 2003; Chavez & Messié, 2009). These ecosystems undergo significant variability at a wide range of frequencies from submonthly to interannual and decadal time scales (Belmadani et al., 2012; Dewitte et al., 2011; Goubanova et al., 2013; Hagen et al., 2001; Junker et al., 2017; Narayan et al., 2010; Pietri et al., 2013; Pizarro et al., 2002; Tim et al., 2015) which substantially impacts the marine resource availability (Echevin et al., 2014; Gomez et al., 2017; Gonzalez et al., 2015; Shannon & O'Toole, 2003; van der Lingen et al., 2006). We focus here on the energetic coastal fluctuations at subseasonal time scales (∼2–120 days), whose signature in Sea Level Anomalies (SLAs) and Sea Surface Temperature (SST) recurrently exceeds ±10 cm and ±2°C respectively within the ∼100 km coastal fringe, adequate for detection using remote satellite observations.

In these EBUS, the coastal subseasonal variability can be associated with the strong oceanic intrinsic variability, characterized by a large variety of mesoscale and submesoscale features (eddies, filaments, and fronts), observed on the distribution of the physical (Chaigneau et al., 2009; Chelton et al., 2011; Morrow et al., 2004) and biogeochemical tracers (Correa-Ramirez et al., 2007; Gruber et al., 2011; Mahadevan, 2014; Marchesiello & Estrade, 2007; Stramma et al., 2013). It is primarily originating from baroclinic instabilities, associated with strong horizontal and vertical shear of the alongshore-current system (Penven et al., 2005). In both systems, these fine scales structures are commonly associated with surface eddy kinetic energy $>100\ cm^2\ s^{-2}$, strong SLA and surface thermal gradients. At a regional scale, subseasonal wind events also trigger significant variations in the upwelling intensity and force poleward-propagating Coastal-Trapped Waves (CTWs). In particular, recent studies showed that in both systems, the subseasonal SST variability, peaking in austral summer, is mainly controlled by alongshore surface winds and heat-flux fluctuations (Bachèlery et al., 2016a; Dewitte et al., 2011; Goubanova et al., 2013; Illig et al., 2014). The latter are associated with migratory atmospheric disturbances across the SEP and St Helena anticyclones.

A specific feature of the coastal SEP and SEA oceans is their relative proximity to the equatorial ocean with a favorable coastal orientation. This makes them particularly sensitive to the oceanic equatorial dynamics associated with eastward propagation of energetic equatorial waves, triggered by trade wind modulation in the western part of the basin (Cravatte et al., 2003; Dewitte et al., 1999, 2003; Illig & Dewitte, 2006, Illig et al., 2004, 2006; Kessler et al., 1995; Rouault et al., 2007). At periods shorter than 2 weeks, mixed Rossby gravity waves dominate the equatorial forcing, while at longer time scales the equatorial connection is mostly due to incoming Equatorial Kelvin Waves (EKWs; Clarke, 1983; Enfield et al., 1987). Upon reaching the eastern basin boundary, part of the equatorial wave energy bounces back along the equatorial waveguide into westward propagating equatorial Rossby waves, while part of incoming energy is transmitted southward along the southwestern coasts of Africa and South America as CTW (Clarke, 1983; Enfield et al., 1987; Moore, 1968). According to the theoretical critical latitude (Clarke & Shi, 1991), at subseasonal frequencies, these coastal waves are trapped along the coast from 5°S (Goubanova et al., 2013; Illig et al., 2014). In this regard, the coastal fringe of the SEP and SEA Oceans can be considered as an extension of the equatorial waveguide.

Using observational data and model outputs, convincing elements have been presented for Kelvin wave propagations from the equator to the coast in the SEP, mostly at interannual time scales and especially during El Niño events (Jacobs et al., 1994; Meyers et al., 1998; Vega et al., 2003). Similarly, in the tropical Atlantic, Grodsky and Carton (2006), Rouault et al. (2007, 2018), and Imbol Koungue et al. (2017) have found coherent interannual variations of SLA in the equatorial Atlantic and the SEA, which are supported by modeling studies (Bachèlery et al., 2016a, 2016b). Further evidence, using SST observations (Picaut, 1983) and tide gauges records (Aman et al., 2007), were also presented in support of interannual coastal wave propagations in the SEA. At subseasonal time scales, SLA data (from altimetry or tide gauges) and current meter measurements, also suggest a clear connection between the equatorial forcing and the coastal variability along the edges of southwestern South American (Clarke & Ahmed, 1999; Enfield et al., 1987; Hormazabal et al., 2002; Leth, 2000; Pizarro et al., 2001, 2002; Shaffer et al., 1997) and African (Goubanova et al., 2013; Polo et al., 2008; Schumann & Brink, 1990) continents. The signature of equatorially forced intraseasonal CTW can be observed in sea level measurement as far south as 30°S off Chile with anomalies larger than ∼10 cm (Hormazabal et al., 2002). These intraseasonal CTW have been shown to significantly amplify the core flow of the Peru-Chile Undercurrent (Shaffer et al., 1997). In the SEA coastal region, the intraseasonal remote oceanic forcing effect can be detected from altimetry only up to 10°S–15°S (Polo et al., 2008). Thus,

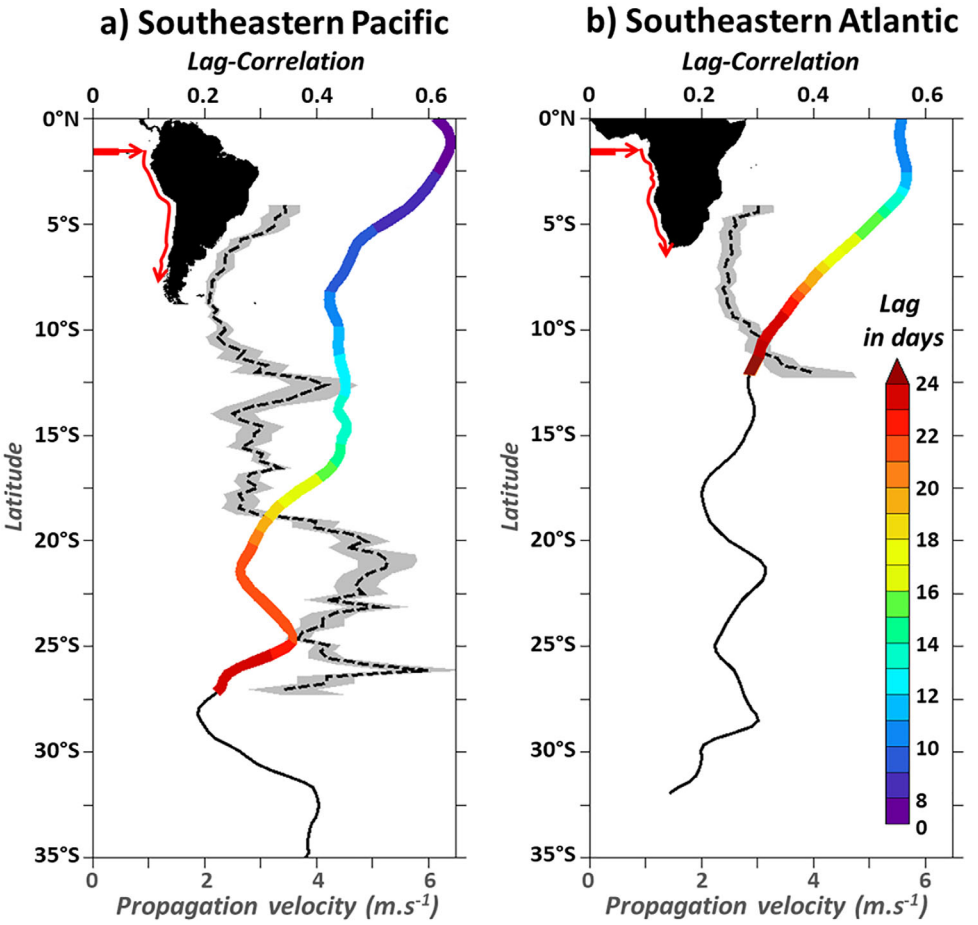

Figure 1. In color: maximum lagged correlation analysis (top scale) between 2000 and 2008 observed (AVISO) coastal (1° coastal band average) Subseasonal Sea Level Anomalies (SSLA) and observed equatorial SSLA averaged within 105°W–95°W; 1°S–1°N and 15°W–5°W; 1°S–1°N in (a) SEP and (b) SEA sectors respectively, as a function of latitude. Lags (in days) are specified with color shading. A positive value indicates that equatorial variability leads. An absence of shading is indicative of a nonstatistically significant correlation coefficient (at 95% level of confidence; Sciremammano, 1979) or to non-monotonically increasing lags when going poleward. Dashed lines: coastal SSLA propagation velocity (m s^{-1}, bottom scale). At each latitude, the maximum lagged correlation between coastal SSLA at this latitude and coastal SSLA within a centered 7° latitudinal window is computed. For each 7°-window, the linear regression coefficient that best fits the lag estimation is calculated. Grey shading indicates error in the linear regression coefficient estimation.

at these frequencies, remotely forced CTW do not reach the Northern Benguela upwelling system (Bachèlery et al., 2016a; Goubanova et al., 2013; Polo et al., 2008). As an illustration, Figure 1 shows the coherence between coastal and equatorial variabilities at subseasonal time scales (∼2–120 days, see section 2.1 for details on the filtering method) is estimated for both systems using altimetric data over the 2000–2008 period. We computed the correlation between the eastern equatorial SLA and the coastal SLA, allowing a lag to account for the coastal wave propagation delay. Results show that the subseasonal equatorial signal remains coherent along the coasts of Peru/Chile up to 27°S, in fair agreement with the results from Hormazabal et al. (2002). Contrastingly, along the coast of western Africa, remotely forced subseasonal poleward propagation are observed no further south than 12°S, in agreement with Polo et al. (2008), Goubanova et al. (2013), and Bachèlery et al. (2016a).

The objective of this study is to explain this striking difference between the two systems regarding the connection with the equatorial variability (Figure 1). We document and compare the characteristics of the remotely forced CTW propagations along the southwestern South American and African continents at subseasonal frequencies. We specifically analyze the key elements of the linear CTW formalism (Brink, 1991; Clarke & Van Gorder, 1986) that can explain such a difference between the two systems; namely, the

amplitude of the equatorial forcing, the dissipation of the CTW modes, and their scattering. Additionally, the subseasonal coastal alongshore wind forcing is also analyzed in both systems, as its contribution is not expected to be in phase with the equatorially forced CTW signal and can thus result in a loss of coherence between coastal and equatorial variabilities. Given the lack of an adequate observation network in the two systems, our approach relies on the numerical experimentation with twin regional ocean general circulation model configurations of the southeastern Pacific and Atlantic Oceans. We benefit from the CTW amplitude extraction methodology developed in the companion paper (Illig et al., 2018), which showed good skills in estimating CTW characteristics from regional ocean models. Our results will be tested using sensitivity experiments with twin configurations of a simple multimode linear CTW model of the two coastal systems.

The paper is structured as follows: section 2 introduces the model configurations and the methodologies. The twin regional ocean general circulation model configurations of the southeastern Pacific and Atlantic Oceans are briefly presented, along with the multimode CTW linear model simulations. We further describe the sensitivity experiments carried out in order to determine to which extent the subseasonal alongshore-current and sea level coastal variability can be accounted for by equatorially remote-forced or locally wind-forced CTW response. Section 3 is devoted to the analysis and the intercomparison of the CTW characteristics (phase speed, magnitude, forcings, dissipation, and scattering) in the southeastern Atlantic and Pacific systems. The last section includes a discussion of the results, followed by concluding remarks and perspectives to this work.

2. Model Configurations and Methodologies

2.1. Climatologies and Anomalies

For the purpose of this study, monthly mean climatologies are estimated over the 2000–2008 period. They are then interpolated onto a daily time axis using cubic splines.

In order to isolate the subseasonal variability, we use the methodology of Goubanova et al. (2013), Illig et al. (2014), and Bachèlery et al. (2016a). Subseasonal anomalies are estimated as the departure from the monthly 1–2–1 weighted average time series. To ensure that no seasonal cycle remains, the monthly mean climatology is also removed. In agreement with Goubanova et al. (2013), submonthly and intraseasonal variability are isolated using a 2–30 days and 30–90 days band-pass Lanczos filter (Duchon, 1979) applied to the subseasonal anomalies. Examples of filtered time series can be found in Goubanova et al. (2013, their Figure 3).

2.2. Subseasonal Equatorial Forcing

Five day averages of SODA 2.1.6 model outputs (Carton & Giese, 2008) are used to quantify the oceanic subseasonal equatorial forcing, responsible for triggering CTW propagations. Note that the coarse temporal resolution of SODA forcing at our disposal prevents the analysis of periods lower than 10 days, and in particular the role of mixed Rossby gravity waves on coastal variability (Enfield et al., 1987).

Eastward propagating EKW amplitudes are estimated using a modal decomposition of the variability (pressure and zonal current). Contributions of the first four EKW modes in the eastern equatorial Pacific and Atlantic Oceans are estimated over the 2000–2008 period by deriving baroclinic mode structures from seasonally and zonally slow-varying stratification over which pressure and zonal current anomalies are projected (Illig et al., 2004). Baroclinic mode contributions are then projected onto the theoretical meridional structures of EKW, accounting explicitly for the coastal boundary near the equator in the Gulf of Guinea (Cane & Sarachik, 1979). EKWs are expressed in terms of the amplitude of contribution to equatorial Subseasonal Sea Level Anomalies (SSLA).

2.3. ROMS Model Twin Configurations

In order to infer and compare the CTW subseasonal characteristics along the coasts of Peru/Chile and southwest Africa, we used the twin regional ocean general circulation model configurations of the southeastern Pacific (from 40°S to 12°N, from 95°W to the South American coast) and the southeastern Atlantic (from 30°S to 7°N, from 10°W to the African coast) developed in the companion paper (Illig et al., 2018). Numerical simulations at 1/12° with 37 sigma vertical levels were performed with the Regional Ocean Modeling System (ROMS; Shchepetkin & McWilliams, 2005) version 3.1 (www.romsagrif.org). Control Run simulations ($ROMS^{CR}$) are forced by 5 day averages of SODA 2.1.6 reanalysis Open lateral Boundary Conditions (OBCs), 0.5° × 0.5° daily QuikSCAT surface wind stress (Blanke et al., 2005), and bulk formulae (Kondo, 1975) using

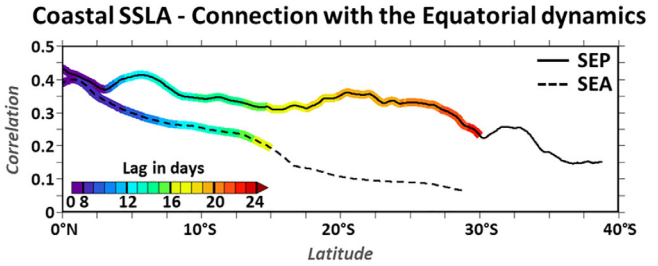

Figure 2. Maximum lagged correlation between ROMS^{CR} coastal (0.5° width band) SSLA and SODA equatorial SSLA as a function of latitude. Plain (dashed) line is for the SEP (SEA) coasts, with equatorial SSLA averaged within 105°W–95°W (15°W–5°W); 1°S–1°N. Lags (in days) are specified with color shading. A positive value indicates that equatorial variability leads. An absence of shading is indicative of a nonstatistically significant correlation coefficient (at 95% level of confidence; Sciremammano, 1979) or to nonmonotonically increasing lags when going poleward.

daily heat and water surface fluxes from ERA-Interim reanalysis (Dee et al., 2011). Simulations were performed over the 2000–2008 period, during which daily averages of temperature, salinity, currents, and sea surface height were stored.

In the companion paper (Illig et al., 2018), the realism of our twin configurations has been evaluated based on a comparison with available satellite and in situ observations. Results show a good representation of the mean state and subseasonal variability. Similar to the altimetric analysis presented in the introduction (Figure 1), the connection with the equatorial signal at subseasonal time scales is investigated in ROMS solutions by estimating the lagged-correlation between *ROMS*^{CR} coastal SSLA and the equatorial variability in the SODA reanalysis at the western boundary of our model domains (Figure 2). Results show that the model is in good agreement with the observations, showing a poleward continuation of the equatorial signal up to 29°S in the SEP and 15°S in the SEA. There are also consistent propagating lags between model and observations that are in agreement with the propagation phase speed estimated in former studies.

2.4. Numerical Experiment Descriptions

Similar to Illig et al. (2014) and Bachèlery et al. (2016a), sensitivity experiments were carried out for both configurations. The purpose is to isolate the propagation of equatorially remote-forced CTW from the impact of the local surface atmospheric forcing variability. These experiments only differ by the surface boundary forcings (wind, wind stress, and heat/freshwater bulk formula fields) which are daily maps in *ROMS*^{CR} experiments (cf., section 2.3) or monthly climatologies in ROMS Equatorial experiments (*ROMS*^{EQ}). Hence, within *ROMS*^{EQ} configuration, assuming some linearity, SEP and SEA subseasonal variability is only impacted by the oceanic remote equatorial connection, while *ROMS*^{CR} is the benchmark experiment in which remote and local forcings are concomitantly at work. Notably, Bachèlery et al. (2016a, 2016b) highlighted the importance of the local atmospheric forcing in the Gulf of Guinea that forces EKW, which in turn trigger CTW that modulate SEA coastal variability. Therefore, $ROMS^{EQ}_{SEA}$ experiment was designed such as the surface atmospheric forcing remains daily in the Gulf of Guinea (north of 4°S and west of 2°E; to reduce spurious wind stress curl, a gradual (linear) 2°-width transition zone is set up between climatological forcing area and the regions where total daily fields are prescribed), while monthly climatological surface atmospheric fields are prescribed elsewhere. Experiment setups and labels are summarized in Table 1.

In order to illustrate the contribution of the equatorial forcing (as simulated by *ROMS*^{EQ}) to the coastal SLA variability (simulated in *ROMS*^{CR}) in both systems, Figure 3 presents the ratio of coastal SLA variance of *ROMS*^{EQ} to *ROMS*^{CR} (shading) and the explained variance of *ROMS*^{EQ} relative to *ROMS*^{CR} (dashed lines). EXPvar, defined as

$$100-100\times\left[\frac{var\left(ROMS^{EQ}-ROMS^{CR}\right)}{var\left(ROMS^{CR}\right)}\right] \quad (1)$$

quantifies the proportion to which *ROMS*^{EQ} is actually in phase and accounts for the variations of the *ROMS*^{CR}, as opposed to variabilities induced by the wind-forcing and model intrinsic non-linearities. At submonthly time scales (grey color in Figure 3) and in the SEP, *ROMS*^{EQ} coastal SLA variance does not exceed 25% of *ROMS*^{CR} coastal SLA variability and its explained variance is almost zero. As reported in Illig et al. (2014), the local atmospheric forcing is thus instrumental in shaping the coastal submonthly variability in the Humboldt system. Contrastingly, in the SEA, a greater amount of the submonthly variability (~50%, along the coast of Angola) is explained by the remote equatorial forcing. Sensitivity experiments to the atmospheric forcing in the equatorial band (not shown) showed that this variability is

Table 1
Description of ROMS Experiments: Domain, Name, Open Lateral Boundary Conditions (OBCs), Surface Forcing Specifications

Domain	EXP-name	OBC	Surface forcing
Southeastern Pacific (SEP)	$ROMS^{CR}_{SEP}$	Total	Total
	$ROMS^{EQ}_{SEP}$	Total	Monthly climatologies
Southeastern Atlantic (SEA)	$ROMS^{CR}_{SEA}$	Total	Total
	$ROMS^{EQ}_{SEA}$	Total	Total within 4°S–7°N; 10°W–4°E and monthly climatologies elsewhere

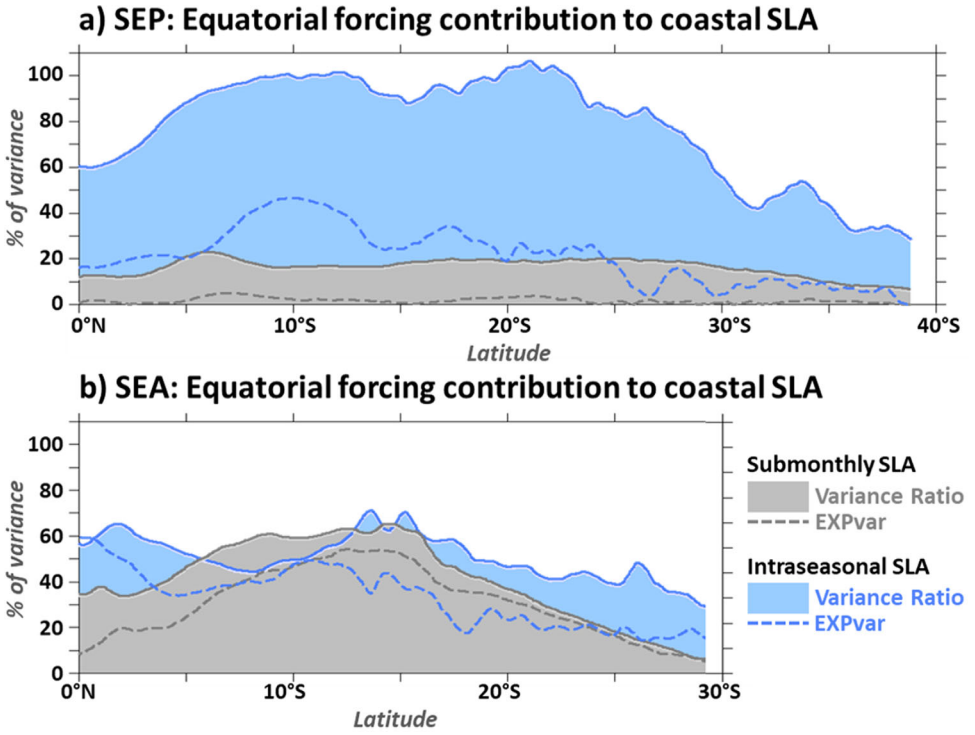

Figure 3. Equatorial remote forcing contribution to coastal SLA (averaged within 0.5° coastal fringe) variability submonthly (grey) and intraseasonal (blue) time scales as a function of latitude in the (top) SEP and (bottom) SEA. Colored shading represents the ratio of variance between $ROMS^{EQ}$ and $ROMS^{CR}$ SLA, while dashed lines show the explained variance of $ROMS^{EQ}$ with respect to $ROMS^{CR}$ (in %, cf., equation (1)).

predominantly forced in the Gulf of Guinea, and associated with first baroclinic mode EKW, in agreement with Figure 12 of Goubanova et al. (2013). Intraseasonal variability (blue color in Figure 3) also exhibits a different behavior in the two basins. In the SEP, while the level of coastal intraseasonal SLA variability remains similar in $ROMS^{EQ}$ and in $ROMS^{CR}$ simulation along the coast of Peru, the explained variance associated with the remote equatorial forcing peaks only at ~50% of $ROMS^{CR}$ variance. Further poleward, $ROMS^{EQ}_{SEP}$ intraseasonal variability gradually decreases and explains less than 10% of $ROMS^{CR}_{SEP}$ coastal intraseasonal SSH variability along the Chilean coast, constantly with the results of Shaffer et al. (1999) and Belmadani et al. (2012). This suggests that from 5°S to 25°S the local atmospheric forcing modulates the coastal variability, while further south it constitutes a source of intraseasonal variability, in agreement with Hormazabal et al. (2001), Illig et al. (2014), and Gomez et al. (2017). In the SEA, $ROMS^{CR}_{SEA}$ intraseasonal variability level and the associated explained variance are maximum close to the equator and decrease poleward. In the Benguela upwelling system, the remote equatorial forcing triggers less than 50% of the coastal intraseasonal variability and explains only ~20% of $ROMS^{CR}_{SEA}$ intraseasonal variability. In agreement with Goubanova et al. (2013) and Bachèlery et al. (2016a), this suggests that in the SEA the local atmospheric forcing triggers a significant part of the intraseasonal coastal SLA variability.

2.5. CTW Contribution to Subseasonal Coastal Variability

A decomposition of the ROMS subseasonal coastal variability into free CTW modes is performed following the new methodology developed and described in the companion paper (Illig et al., 2018). At all cross-shore sections along the southwestern African and South American continents, every 1/12°, CTW modal structures of the first four free CTW modes are derived using ROMS mean (2000–2008) stratification and topography by applying the Brink and Chapman (1987) Coastal-Trapped Wave programs. Subseasonal model pressure anomalies are then projected onto these structures based on the modal structure orthonormal conditions (Brink, 1989). As described in the companion paper (Illig et al., 2018), this methodology has shown good skills in estimating CTW characteristics in both systems. In this paper, CTW are expressed in terms of their contribution to subseasonal SLA and alongshore-current anomalies.

Table 2
Description of LCM Experiments Conducted With SEP and SEA Configurations: Name, Equatorial Forcing, Alongshore Wind Stress Forcing (ASWS), and Wave Dissipation/Scattering Specifications

EXP-name	EKW forcing	ASWS forcing	Dissipation	Scattering
LCM^{EQ}_{noDISS}	Total	None	No	No
LCM^{EQ}_{noSCAT}	Total	None	Yes	No
LCM^{EQ}	Total	None	Yes	Yes
LCM^{CR}	Total	Total	Yes	Yes

Results of this analysis will provide useful information to compare the characteristics of each subseasonal CTW mode in both systems in order to explain the differences in the coastal variability regarding the consistency with the equatorial variability (Figures 1 and 2). We will then discuss our results in the light of the multimode linear CTW model simulations carried out for the two coastal systems and described in the following section.

2.6. Linear CTW Simulations

In both systems, simulations with the linear coastal model (LCM) twin configurations of the southeastern Pacific and the southeastern Atlantic developed in the companion paper (Illig et al., 2018) have been carried out, following the algorithm of Clarke and Van Gorder (1986). LCM consists in the propagation of the four gravest CTW modes, whose amplitude varies along the coast and in time ($\phi_n(y,t)$) and satisfies

$$(\phi_n)_y - \frac{1}{c_n}(\phi_n)_t + a_{nn}\phi_n = b_n\tau^A - \sum_{\substack{m=1 \\ m\neq n}}^{+\infty} a_{mn}\phi_m \quad (2)$$

where subscripts y and t represent partial differentiation. Model parameters, namely, CTW phase speed (c_n), frictional decay coefficient (a_{nn}), frictional coupling coefficient ($a_{\substack{mn \\ n\neq m}}$), and wind projection coefficient (b_n) are derived using the CTW modal decomposition outputs (eigenvalues and eigenfunctions, cf., section 2.5) following the formulae from Clarke and Van Gorder (1986) which are recalled in the companion paper (Illig et al., 2018). They vary latitudinally with the wave propagation. Alongshore subseasonal wind stress forcing ($\tau^A(y,t)$) comes from daily QuikSCAT product (Blanke et al., 2005). SEP and SEA coastal waveguides are sampled every ~5 km and model parameters remain uniform for each 0.5° length of coastal section. CTW are forced at the equator by the 5 day SODA EKW mode subseasonal contributions (see section 2.2).

Sensitivity experiments to the model parameters and alongshore subseasonal wind stress forcing were conducted. In LCM^{EQ}_{noDISS} experiment, CTW modes are forced at the equator and propagate freely to the southern boundary of LCM domains, without dissipation ($a_{mn}=0$) and local wind stress forcing ($b_n=0$). In LCM^{EQ}_{noSCAT} and LCM^{EQ} frictional dissipation ($a_{nn} \neq 0$) and scattering ($a_{\substack{mn \\ n\neq m}} \neq 0$) are subsequently introduced in the LCM (equation (2)). LCM^{CR} is the most realistic experiment in which frictional dissipation, coupling between modes and coastal wind stress forcing are at work. Experiment setups and labels are summarized in Table 2.

3. Results: Intercomparison of the CTW Dynamics in SEP and SEA

Our main purpose is to explain the similarities and differences between SEP and SEA systems regarding the connection with the equatorial variability at subseasonal time scales. The analysis of altimetric data (Figure 1) and $ROMS^{CR}$ outputs (Figure 2) clearly highlights that equatorially forced CTW can be tracked up to ~30°S in the Humboldt Current system (SEP). In contrast, in the SEA, the consistency with the equatorial dynamics fades at ~12°S, off central Angola. To explain this difference, we will analyze the equatorial forcing, and compare between each basin, the characteristics of CTW propagations (vertical structures, phase speed, amplitude, dissipation rate, and modal scattering). We will also address the role of the local wind stress forcing.

3.1. Remote Equatorial Forcing Characteristics

First, this difference in the subseasonal coastal dynamics between the two basins might be directly linked to the amplitude of the equatorial forcing in the eastern equatorial Pacific (EEP) and Atlantic (EEA). Therefore, we compare the amplitude of the subseasonal EKW modes between the EEP (averaged within 105°W–95°W; 1°S–1°N, Figure 4a) and the EEA (averaged within 5°W–5°E; 1°S–1°N), Figure 4b) sectors. Since most of the equatorial variability projects on the gravest baroclinic modes (Dewitte et al., 1999; Illig et al., 2004), we have quantified the EKW contribution to SSLA of the first three baroclinic modes (cf., section 2.2). These modes are expected to propagate farther, as they are faster and less dissipative than higher-order modes. We have computed the root-mean-square (RMS) of individual EKW and their summed-up contribution at subseasonal frequencies (see white histograms in Figure 4). Results show that there is no striking difference in the amplitude of the total propagating subseasonal equatorial variability between the two sectors. In the

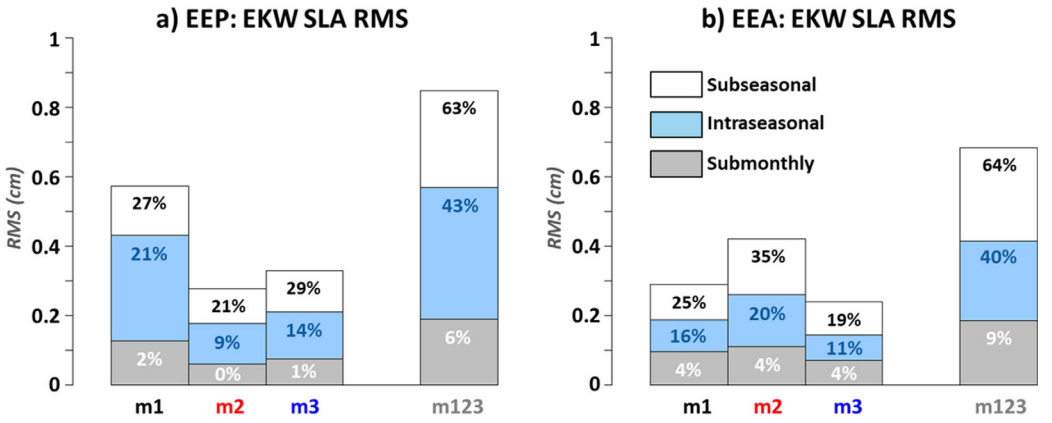

Figure 4. Histogram of SODA Equatorial Kelvin Wave (EKW) SLA root-mean-square (RMS, in cm) for the three gravest baroclinic modes and their summed-up contribution in (a) the eastern equatorial Pacific (EEP, averaged within 105°W–95°W; 1°S–1°N) and (b) in the eastern equatorial Atlantic (EEA, averaged within 5°W–5°E; 1°S–1°N) for subseasonal (white), intraseasonal (blue), and submonthly (grey) time scales. For each frequency band and each baroclinic mode, the percentage listed corresponds to the explained variance of the EKW SLA contribution to SODA subseasonal SLA (in %, cf., equation (1)).

EEA, the SSLA RMS of the summed-up contribution of the three gravest EKW modes is only 20% smaller than in the EEP. However, the contribution of each baroclinic mode is distinct in the two basins. In the EEP, the first baroclinic mode is the most energetic (explaining 27% of the EEP SSLA), while the second baroclinic mode carries less energy than the third one (in agreement with Dewitte et al. (2008)). In the EEA, the second baroclinic mode is dominant (explaining 35% of the EEA SSLA; in agreement with Illig et al. (2004)) and its RMS is 1.6 times larger than in the EEP. The first and third EKW modes are considerably weaker in the EEA than in the Pacific counterpart, their amplitude being half that of the ones in the EEP. These distinct distributions of the EKW contributions between the two basins remain almost the same at submonthly and intraseasonal time scales (grey and blue histograms in Figure 4).

In conclusion, the subseasonal equatorial forcing is not substantially stronger in the EEP compared to the EEA, to explain the 15° difference observed between the two systems in the maximum latitude at which the coastal variability remains consistent with the equatorial forcing (Figures 1 and 2). But important differences exist in the amount of energy carried by the first two baroclinic modes which may explain the distinct coastal dynamics of each system. This will be investigated in the following sections by comparing the CTW characteristics of each mode between the two basins.

3.2. CTW Modal Structures

We compute CTW modal structures along the coasts of Peru/Chile and Western Africa. Their shape, determined by ROMS cross-shore topography and mean offshore stratification profile (companion paper Illig et al., 2018), controls the amplitude of critical CTW parameters (wave speed, dissipation, and wind projection coefficient, section 2.6). In this context, the Burger number S (Huthnance, 1978), defined as $S=\alpha\bar{N}/f$, provides a measure of the relative importance of the cross-shore topography slope (α), the mean offshore stratification ($\bar{N}$), and the Coriolis force (f). For $S^2 \geq O(1)$, CTW are affected by the stratification and respond baroclinically. Small S^2 values ($S^2 \ll 1$) correspond to waves affected mainly by topography and approach barotropic continental shelf waves (Brink, 1987). Given the differences in bathymetry and stratification along the coasts of SEP and SEA (Figure 5 and Table 3), differences in CTW modal structures are expected. In the SEP, the mean stratification (averaged within the upper 3,000 m) remains constant (0.22–0.23 s^{-1}) along the coast of South America (blue line in Figure 5a). In the SEA, $\bar{N}$ slightly decreases from 0.25 s^{-1} at 5°S to 0.22 s^{-1} at 16°S and remains constant further south (blue line in Figure 5b). The most drastic difference between the two regions lies in the shape of the coastal bathymetry. In the SEP, the bathymetry is steeper than in the SEA, frequently exceeding 5,000 m depth within the first 150 km offshore. The gradients of the continental slope are maximum between 3,000 and 4,000 m depth, with an average (between 5°S and 38°S) of ~85 m km^{-1}, peaking up to 140 m km^{-1} along the coast of Northern Chile. In the SEA sector, the slope is substantially gentler. The gradients are maximum between 1,000 and 2,000 m depth, ~18

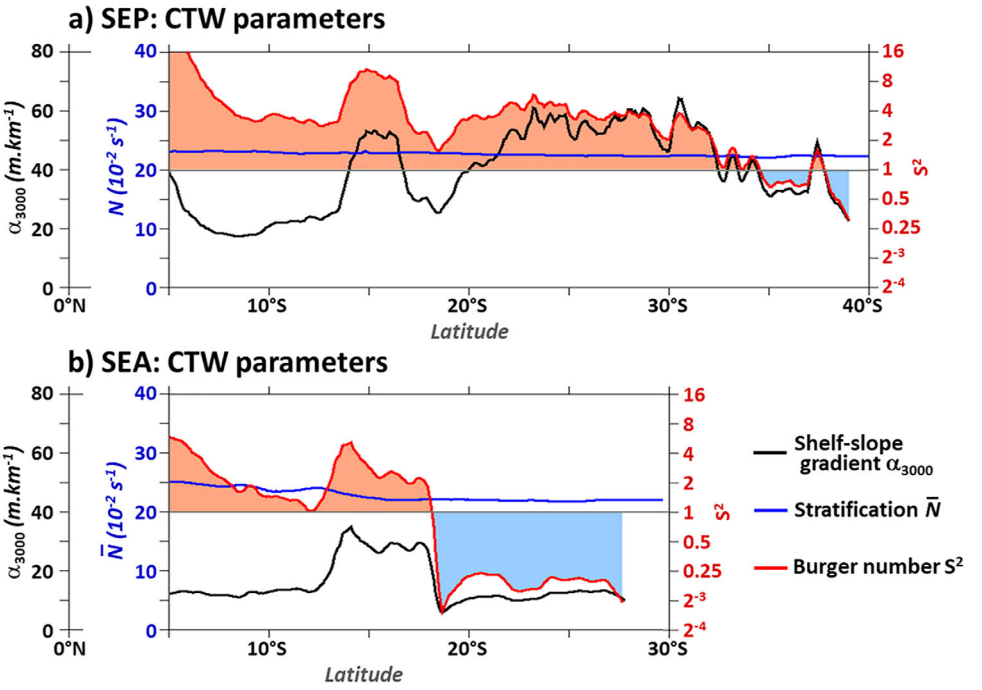

Figure 5. Parameters controlling CTW vertical structures in function of latitude along the coasts of the (top) SEP and (bottom) SEA Oceans. α is representative of the shelf-slope gradient (black lines, $\alpha_{3000}=3,000/L_{3000}$, where L_{3000} is the distance between the coast and the 3,000 m isobath, unit is m km^{-1}, black left scale). $\bar{N}$ is the mean buoyancy frequency averaged within the upper 3,000 m (blue lines, unit is 10^{-2} s^{-1}, blue left scale). $S^2=(\alpha\bar{N}/f)^2$ is the squared Burger number (red lines, unitless, red right scale). To better visualize $S^2 \gg 1$ and $S^2 \ll 1$, we use a log 2 vertical scale. Red and blue shadings correspond to S^2 values larger and lower than 1.

m km^{-1} on average between 5°S and 27°S. The 3,000 m isobath is situated at ~200 km offshore north of 13°S and south of 18°S. Notably, steeper slopes (>60 m km^{-1}) are observed north of the Angola Benguela Frontal Zone (ABFZ) between 13°S and 17°S. To summarize and compare coastal bathymetric profiles on the shelf and slope of both regions, we defined a topographic slope index ($\alpha 3,000$) as the ratio between the depth 3,000 m and the distance from the coast at which the 3,000 m isobath is encountered ($\alpha_{3000}=3,000/L_{3000}$). $\alpha 3,000$ portrays the bathymetric profiles described previously (black line in Figure 5). The combined effect of stratification, topography, and latitude (through f) affecting the CTW nature are then quantified through the estimation of S^2. Results show that large values of S^2 are encountered along the SEP coast (Figure 5a), especially off central Peru. Lower S^2 values are estimated along Southwest Africa and in particular in the Northern Benguela upwelling system (Figure 5b). Increasing latitude also favors small S^2 values associated with barotropic structures (Brink, 1982), especially along the South Chilean coast.

Pressure modal structures of the four gravest CTW modes are derived from ROMS mean stratification and topography along the southwestern coasts of the South American and African continents (cf., section 2.5).

Table 3
Parameters Controlling CTW Vertical Structures at 16°S and 27°S Along the Coasts of Southwestern South America and Africa

Sector	Latitude (°S)	f (10^{-5} s^{-1})	$\bar{N}$ (10^{-4} s^{-1})	L_{3000} (km)	α (m km^{-1})	S^2
SEP	16	−4.0	22.8	59.64	50.3	8.22
	27	−6.6	22.9	58.37	51.4	3.06
SEA	16	−4.0	22.05	101.8	29.5	2.62
	27	−6.6	22.02	227.8	13.2	0.19

Note. f is the Coriolis frequency at the coast, $\bar{N}$ is ROMS mean (2000–2008) buoyancy frequency averaged within the first 3,000 m, L_{3000} is the distance between the 3,000 m isobath and the coast, α is representative of the shelf-slope gradient ($\alpha_{3000}=3,000/L_{3000}$), and $S^2=(\alpha\bar{N}/f)^2$ is the squared Burger number.

Examples of CTW pressure structures are shown in Figures 3 and 12 of the companion paper (Illig et al., 2018) for cross-shelf sections along the Peruvian (16°S) and Namibian (27°S) coasts. According to the Burger number estimations associated with the deep and steep bathymetry along the Peruvian/Chilean coasts (Figure 5), the CTW modal structures are baroclinic, with isopleths slanting outward. The modal structure and phase velocity of the gravest CTW mode approach the characteristics of a deep ocean internal Kelvin wave (consistently with Brink (1982)). Conversely, in the Benguela upwelling system, modal structures show nearly vertical isopleths over the shelf and slope, consistent with nearly barotropic dynamics associated with small S^2 values. Accordingly, phase speed values are larger in SEA than in SEP and latitudinal variations of the phase speed (Figure 4 of the companion paper (Illig et al., 2018)) are inversely proportional to S^2 values.

3.3. CTW Mode Contribution to Coastal Subseasonal Variability

By projecting ROMS pressure subseasonal anomalies onto the CTW modal structures, we estimate the amplitude of the first four CTW modes (cf., section 2.5), following the methodology validated in the companion paper (Illig et al., 2018). The contribution of each CTW and their summed-up contribution to the coastal SSLA and Subseasonal Alongshore Current Anomalies (SASCA) are quantified in the SEP and SEA. Figures 7c and 7d of the companion paper (Illig et al., 2018) present the coastal SSLA RMS of the first four CTW modes. Here Figure 6 presents their explained variance relative to the coastal SSLA and SASCA

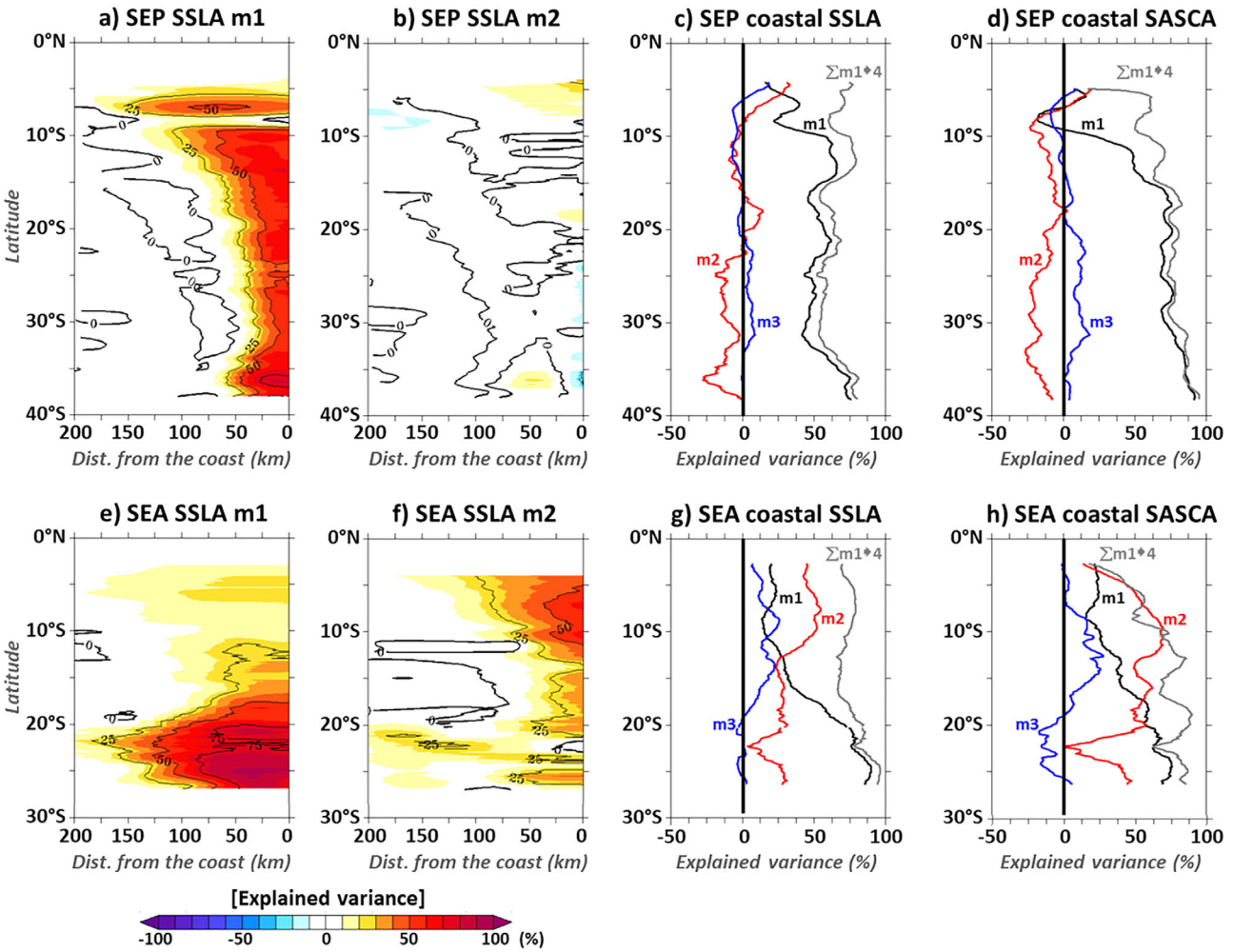

Figure 6. CTW mode contribution (explained variance in %, cf., equation (1)) to SSLA and SASCA along the coasts of the (top) SEP and (bottom) SEA Oceans. (a/e) The explained variance of the first CTW mode contribution to model SSLA, as a function of the distance from the coast (km) and the latitude. (b/f) The explained variance of the second CTW mode contribution to model SSLA, as a function of the distance from the coast (km) and the latitude. (c/g, e/f) The explained variance of the first three CTW modes and the summed-up contribution of the four gravest CTW modes to coastal SSLA (averaged within 0.5° coastal fringe) and SASCA (averaged within 100 km/200 m depth coastal fringe), respectively.

variability. In agreement with the shape of the CTW modal structures, the maximum amplitude of the modes is trapped at the coast. In both systems, the summed-up contribution of the four gravest CTW modes explains more than 50% of the coastal SSLA variability (grey lines in Figures 6c and 6g), emphasizing the importance of the subseasonal CTW dynamics in the coastal fringe. North of 7°S (10°S) in the SEP (SEA), the alongshore-current dynamics is more complex and cannot be explained purely by the summed-up contribution of the gravest CTW modes (grey lines in Figures 6d and 6h). Results also show that there are important differences in the relative contribution of each CTW mode between the two basins. In agreement with the characteristics of the remote equatorial forcing, CTW mode 1 is dominant in the SEP. It explains more than 50% of the coastal (0–50 km) SSLA and SASCA variability over much of the coast (Figure 6a and black line in Figures 6c and 6d), showing a local minimum near 8°S. The contribution of the second CTW mode remains very weak, except north of 6°S, where its contribution is comparable to the one of the first CTW mode (Figure 6b and red line in Figures 6c and 6d). In contrast, in the SEA, the second CTW mode is the most energetic north of ∼13°S, while poleward, the first CTW mode dominates the subseasonal coastal variability (Figure 6 lower panels). These differences between the two systems in terms of the relative contribution of each CTW mode are in agreement with the dynamics of the linear coastal model (cf., Figures 10c and 10d and Figures 7a and 7b of the companion paper (Illig et al., 2018)).

In conclusion, the dynamics in the SEP is straightforward: the subseasonal equatorial forcing, consisting of the dominant first EKW mode, is transmitted southward along the coasts of Peru/Chile as a first CTW mode. This mode remains dominant along the entire coast of western South America, enabling a consistency with the equatorial variability at high latitudes. In the SEA, the second EKW carries most of the subseasonal equatorial forcing. Its energy is transmitted poleward along the southwestern coast of Africa as a second CTW mode. However, its contribution to the coastal subseasonal variability drastically diminishes between 12°S and 15°S, where CTW mode 1 amplitude increases. This transition in the dominance between the two gravest CTW modes corresponds exactly to the latitude where the connection between coastal and equatorial variabilities fades out (Figures 1b and 2). In the following section, we will investigate the processes that explain the fading of the SEA second CTW mode.

3.4. CTW Frictional Dissipation

Along their propagations, CTW modes experience dissipation and scattering due to bottom friction (equation (2)). CTW frictional decay coefficients (a_{nn}) and frictional coupling coefficients ($a_{\substack{mn\\n\neq m}}$) are estimated in the SEP (Figures 7a and 7b) and SEA (Figures 7c and 7d), based on CTW eigenfunction values (cf., Clarke & Van Gorder, 1986 and equation (7) of the companion paper (Illig et al., 2018)). Coefficients are represented using a matrix, such as the amplitude of a given CTW mode of order n will be affected by the amplitude of a mode of order m through the frictional coefficient a_{mn} (equation (2)). Diagonal elements are the frictional decay coefficients (a_{nn}). Coefficients have been averaged over 5° latitudinal bands, within 5°S–10°S, where CTW mode 2 is dominant in the SEA, and further south within 20°S–25°S, where the contribution of SEA CTW mode 1 becomes dominant. Results show that in both systems and at all latitudes along the coasts, higher-order CTW modes dissipate more strongly than gravest modes (diagonal values in Figure 7). Also, for each CTW mode the dissipation is stronger in the SEA than in the SEP (average within 5°S–25°S, not shown). As a consequence, the SEA dominant CTW mode 2 which carries the equatorial forcing signal will dissipate considerably faster than the SEP remotely forced CTW mode 1. Between 5°S and 10°S, the alongshore decay scale of the second CTW mode (a_{22}^{-1}) in the SEA is 714 km, while in the SEP, a_{11}^{-1} is equal to 2,564 km.

This suggests that CTW frictional dissipation may explain the early fading of the coherence between coastal and equatorial subseasonal variabilities in the SEA compared to the SEP sector. This hypothesis is further tested out using the SEP and SEA linear coastal model configurations (cf., section 2.6). We performed two sensitivity experiments (cf., Table 2) in which subseasonal CTW are forced at the equator but are not impacted by the coastal wind stress forcing ($b_n=0$ in equation (2)). They differ by the way friction affects CTW propagations: LCM^{EQ}_{noDISS} is the frictionless case ($a_{nn}=a_{\substack{mn\\n\neq m}}=0$ in equation (2)) and in LCM^{EQ}_{noSCAT}, CTW dissipate along their propagation ($a_{nn}\neq 0$) without modal scattering ($a_{\substack{mn\\n\neq m}}=0$). In these experiments, Figure 8 shows the contribution of the CTW modes to the coastal SSLA. The latitudinal variations of the CTW eigenfunctions ($F_n(x=0,z=0)$) are thus superimposed on top of the variations of the amplitude of the modes (ϕ_n), which can give the false impression that CTW modes dissipate less in the SEA than in the SEP. As expected, in the frictionless case (not shown), CTW propagate straightforwardly up to the southern boundary of both domains. In agreement with the equatorial forcing characteristics (Figure 4), in the SEP (SEA),

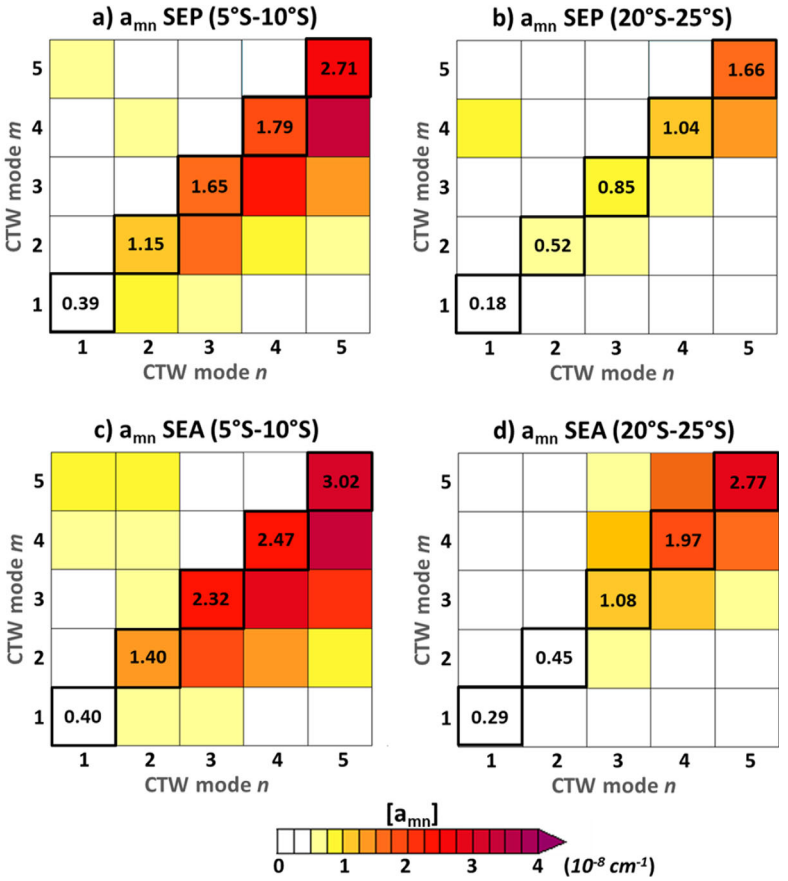

Figure 7. Frictional coefficients (a_{nm}, in 10^{-8} cm^{-1}) along (a) North Peruvian (averaged within 5°S–10°S), (b) the North Chilean (averaged within 20°S–25°S), (c) along North Angolan (averaged within 5°S–10°S), and (d) Namibian (averaged within 20°S–25°S) coasts.

CTW mode 1 (2) remains the most energetic all along the coast. The coherence between coastal and equatorial variabilities remains strong up to 40°S (30°S) in the SEP (SEA). When introducing the CTW linear dissipation, the amplitude of the weakly dissipative first CTW mode remains strong all along the coasts of both basins (black lines in Figures 8a and 8b), while the amplitude of the higher-order modes decreases rapidly, in particular in the SEP. There, the coherence with the equatorial variability, estimated by the maximum lag correlation between equatorial SSLA forcing (summed-up contribution of the 4 CTW modes) and the LCM coastal SSLA, remains prominent until the southern boundary of the model domain. In the SEA, CTW mode 2 energy decreases along its propagation, to reach the level of the amplitude of the first CTW mode around 15°S, in agreement with ROMS solutions (Figure 6). The coherence with the equatorial forcing is high (correlation > 0.7) until 30°S, but lags are not monotonically increasing south of 19°S (dashed line without shading in Figure 8b). This latitude is however too far south compared to the 12°S–15°S latitude estimated with altimetry (Figure 1).

3.5. CTW Modal Scattering Due to Bottom Friction

Bottom friction also triggers modal scattering (equation (2) and Clarke and Van Gorder (1986)) which can contribute to the decrease in the consistency between coastal and equatorial variabilities. In Figure 7, the largest values of frictional coupling coefficients $a_{\substack{mn \\ n \neq m}}$ are found below the diagonal of the frictional coefficient matrix, implying that the magnitude of a given mode of order n will be affected by the amplitude of lower order modes ($m < n$). As a result, in both systems, CTW mode 1 will hardly be impacted by higher-order modes. In the Namibian upwelling system, the frictional coefficient matrix becomes symmetric (Figure 7d), characteristic of barotropic CTW modal structures (see Clarke & Van Gorder, 1986, Appendix A.2). On average within 5°S–25°S, the modal scattering is stronger in the Atlantic than in the Pacific, for each CTW mode.

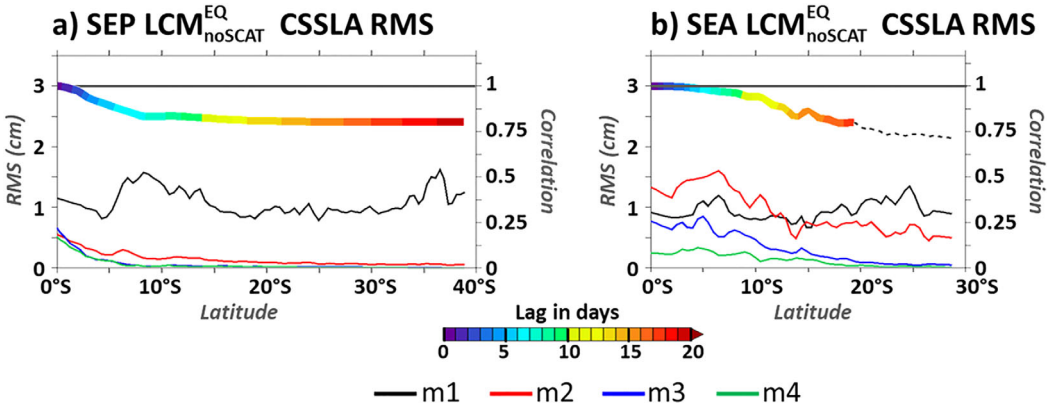

Figure 8. LCM^{EQ}_{noSCAT} CTW mode contribution to coastal (0.5° width band) SSLA (CSSLA) along the coasts of the (a) SEP and (b) SEA. Root-mean-square of CTW modes 1–4 are in black, red, blue, and green plain lines, respectively. Unit is cm. Maximum lagged correlation between equatorial and coastal SSLA as a function of latitude, with monotonically increasing lags (in day) is specified with color shading. A positive value indicates that equatorial variability leads.

This is all the more true in the SEA, where the remote forcing signal is dominated by the second CTW mode. Its amplitude will be impacted by the amplitude of the first CTW mode (Figure 7c), which still explains ∼25% of the coastal variability (Figure 6e).

The role of modal scattering in the loss of coherence between coastal and equatorial variabilities is quantified using the LCM. We conducted an additional sensitivity experiment, LCM^{EQ} (Table 2), in which frictional dissipation and scattering are at work ($\forall n, \forall m, a_{mn} \neq 0$ in equation (2)). Compared to LCM^{EQ}_{noSCAT} results basins (Figures 8a and 8b), in LCM^{EQ} the level of correlation between equatorial and coastal variabilities decreases in both basins (Figures 9a and 9b). Concomitantly, the amplitude of CTW modes 2–4 increases. Notably, in both basins, the amplitude of CTW mode 1 is barely affected by the scattering, except south of 34°S (19°S) in the SEP (SEA), where CTW modal structures become barotropic (Figure 5) and frictional coupling coefficients increase (Figures 7b and 7d). The coherence with the equatorial forcing still remains strong until 40°S in the SEP, while it stops at 14°S in the SEA, in agreement with the observations (Figure 1) and ROMS^{CR} simulation (Figure 2). Notably, scattering do not explain the increase of the first CTW mode in the SEA south of ∼13°S (Figure 6e).

So far, accounting for the differences in subseasonal equatorial forcing in each basin, CTW frictional dissipation and scattering explain the early fading of the connection between coastal and equatorial subseasonal variabilities in the SEA compared to the SEP. However, these processes do not trigger the loss of coherence between coastal and equatorial variabilities around 30°S in the SEP (Figures 1 and 2) nor the increase of the first CTW mode subseasonal variability south of ∼13°S in the SEA. Since the local atmospheric forcing

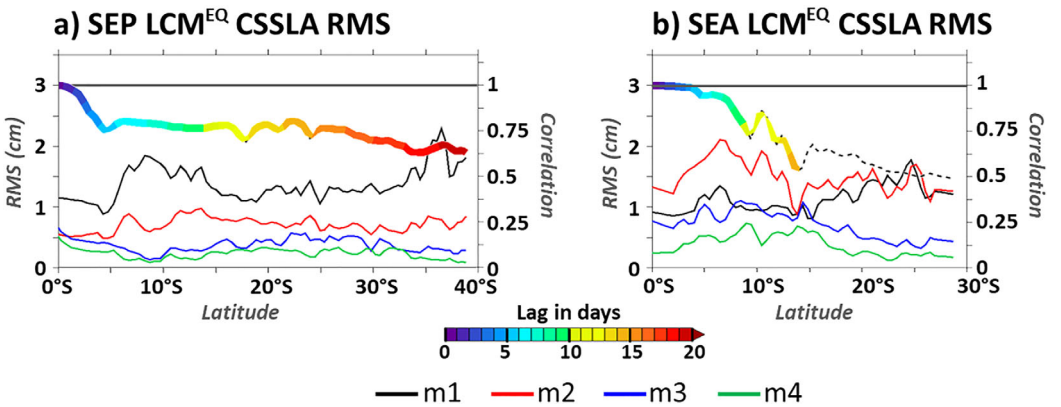

Figure 9. Same as Figure 8 but for LCM^{EQ} simulation.

triggers a significant part of the subseasonal coastal variability (section 2.4 and Figure 3), we will now investigate its impact on the CTW dynamics.

3.6. Local Subseasonal Forcing Contribution

Along their propagations, CTW are also forced by subseasonal alongshore wind stress (equation (2)). Its variability is not expected to be phased with the equatorial forcing, which can decrease the coherence between coastal and equatorial variabilities. The amplitude of the alongshore submonthly (grey) and intraseasonal (blue) coastal wind stress variability is presented in Figure 10a, along the coasts of SEP (shading) and SEA (dashed lines). Results show that subseasonal wind stress (summed-up contribution of submonthly and intraseasonal fluctuations) is more energetic in the Atlantic than in the Pacific, in particular, south of 15°S. This is also true for submonthly and intraseasonal frequency bands taken separately.

Coastal wind stress energy is projected onto individual CTW modes according to the wind projection coefficient b_n (equation (2)). The four gravest CTW wind projection coefficients (Figure 10 bottom) are estimated in the SEP (bright colors) and in the SEA (light colors) based on CTW eigenfunction values (cf., Clarke & Van Gorder, 1986 and equation (8) of the companion paper (Illig et al., 2018)). Similar to Figure 7, coefficients have been averaged over 5° latitudinal bands; namely, within 5°S–10°S (Figure 10b), where CTW mode 2 is dominant in the SEA and wind stress variability remains weak; within 15°S–20°S (Figure 10c), which is at the transition between dominant CTW modes 2 and 1 in the SEA and where alongshore wind stress becomes energetic; and within 25°S–30°S (Figure 10d), where the alongshore wind stress is energetic in both basins.

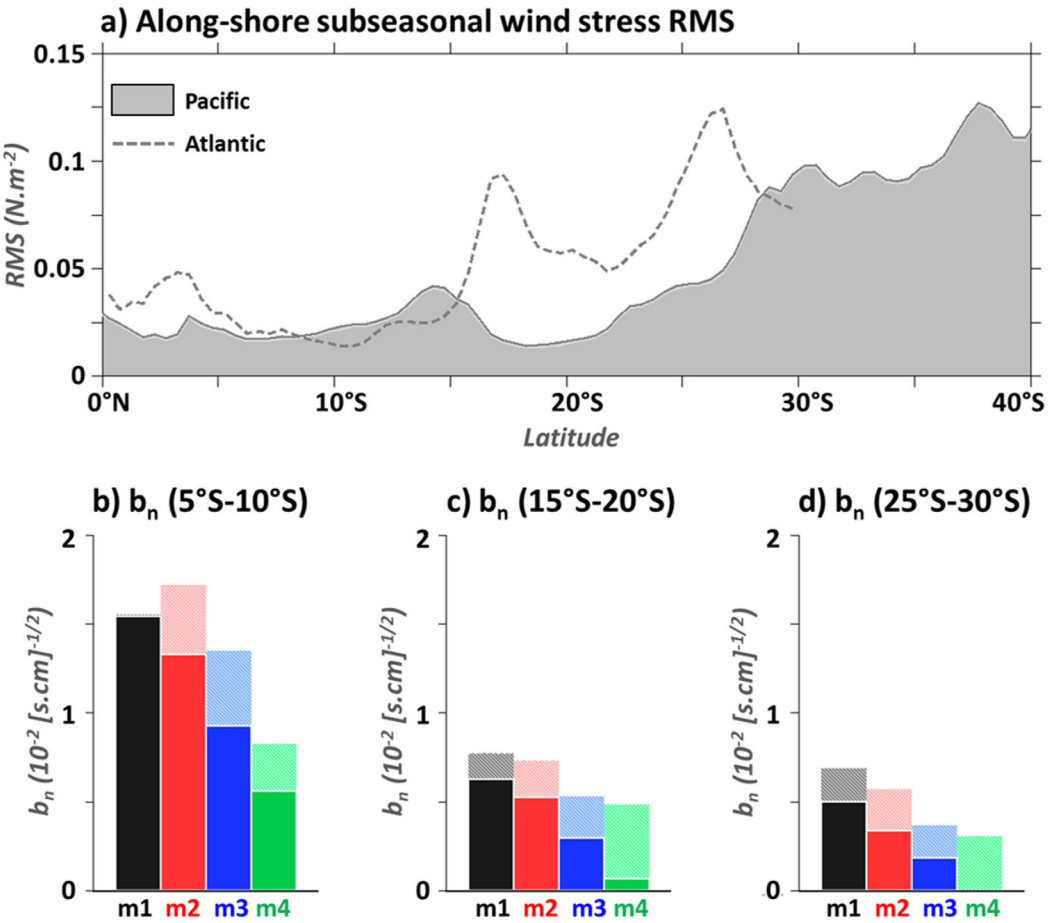

Figure 10. (a) Root-Mean-Square (RMS) of QuikSCAT alongshore wind stress (N m^{-2}) for subseasonal time scales in function of latitude along the coasts of the SEP (shading) and SEA (dashed lines) oceans. (b) Histogram of the wind projection coefficient (b_n, in 10^{-2} (s cm)$^{-1/2}$) for the four gravest CTW modes in the southeastern Pacific (bright shading) and Atlantic (light shading) Oceans, averaged within (left) 5°S–10°S, (middle) 15°S–20°S, and (right) 25°S–30°S.

Results show that on average (5°S–30°S), wind projection coefficients are larger in the Atlantic than in the Pacific for all the CTW modes. This has to be attributed to the shape of the cross-shore topography in the coastal fringe that controls the nature of the CTW structures (cf., section 3.2). The shallower and gentler bathymetry off southwestern Africa compared to the one in the SEP sector yield more barotropic CTW, associated with larger wind projection coefficients especially south of 20°S. This will all the more increase the impact of the larger SEA subseasonal wind stress fluctuations onto the CTW propagation compared to the SEP. Notably, where subseasonal coastal wind variability is strong (south of 25°S [15°S] in the SEP [SEA]), local wind stress forcing will project preferentially onto the first CTW mode.

The role of the subseasonal wind stress forcing is further quantified in each system based on sensitivity experiments with ROMS (Table 1) and LCM (Table 2) model. We compare coastal SSLA from simulations in which no subseasonal wind stress forcing is prescribed (dashed line in Figures 11a and 11b for ROMS^{EQ} and Figure 9 for LCM^{EQ}) to control run simulations (plain lines in Figures 11a and 11b for ROMS^{CR} and Figures 11c and 11d for LCM^{CR}). In agreement with the wind projection coefficients (Figures 10b–10d), model results show that the alongshore wind stress primarily impacts the amplitude of CTW mode 1 in both basins. Also, consistently with the subseasonal wind stress magnitude (Figure 10a), CTW mode 1 amplitude is substantially increased south of 25°S (15°S) in the SEP (SEA) when adding the contribution of the local atmospheric forcing. Notably, ROMS and LCM simulations agree well in that matter, showing comparable amplitudes of CTW modes 1 and 2 (Figure 11). Furthermore, subseasonal coastal wind stress also impacts the strength of the coherence between coastal and equatorial variabilities. The maximum lag-correlation coefficient is indeed considerably decreased from LCM^{EQ} (Figure 9) to LCM^{CR} (Figures 11c and 11d), in better agreement with the observations (Figure 1). In LCM^{CR} and ROMS^{CR} (Figure 2), the coherence with the equatorial variability remains significant until 30°S (~14°S) in the SEP (SEA), in agreement with the altimetry (Figure 1). Finally, Figure 12 presents the SEP and SEA power spectrum analysis of ROMS^{EQ} (lines) and ROMS^{CR} (shadings) CTW mode 1. The spectral density for long-wave coastal propagations is obtained by summing-up only the

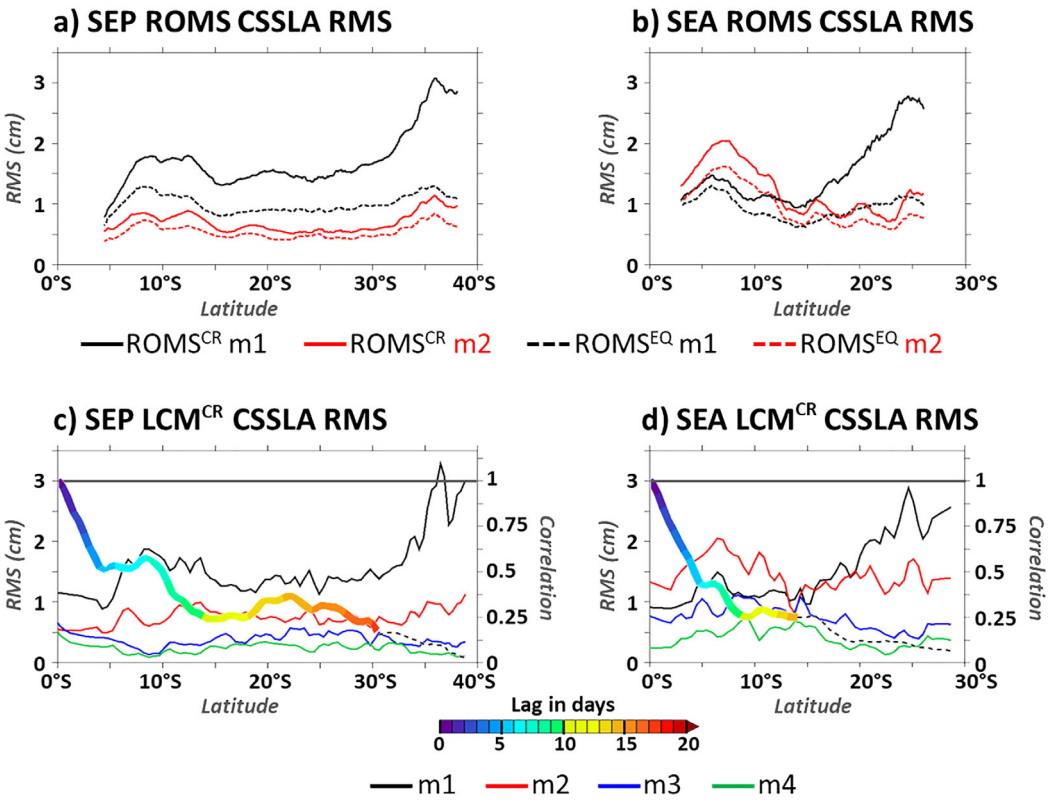

Figure 11. (top) Root-mean-square of CTW mode contribution to coastal (0.5° width band) SSLA (CSSLA, cm) along the (a) SEP and (b) SEA coasts for ROMS^{CR} (plain lines) and ROMS^{EQ} (dashed lines) simulations. CTW mode 1 is in black and CTW mode 2 is in red. (bottom) Same as Figure 8, for LCM^{CR} along the (c) SEP and (d) SEA coasts.

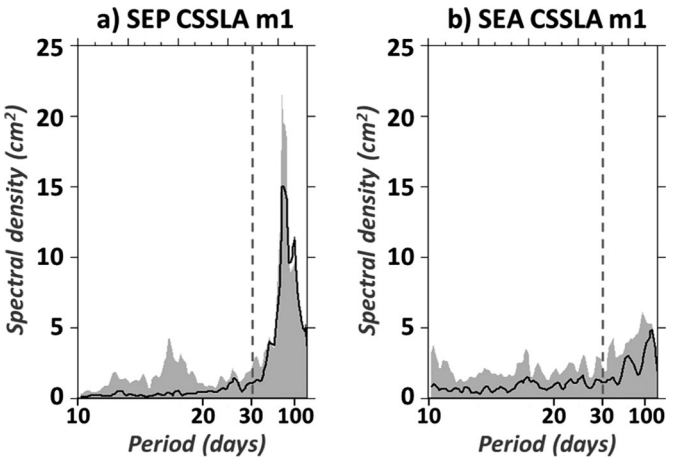

Figure 12. Space-time power spectra (Hayashi, 1982) summed over long spatial scales (>5° of latitude) for ROMS^{CR} (grey shading) and ROMS^{EQ} (black line) CTW mode 1 coastal SSLA (CSSLA) in the (a) SEP and (b) SEA oceans. In the SEP (SEA), the analysis is performed within a 32°-length (24°-length) domain extending from 3°S to 35°S (from 3°S to 27°S). Unit is cm^2. Grey dashed vertical lines indicate the separation between submonthly and intraseasonal frequencies.

long spatial scales (>5° in latitude) of a Hayashi (1982) space-time analysis (cf., Figure 10 of the companion paper (Illig et al., 2018)). Results show that, in the SEP, the local atmospheric forcing primarily impacts submonthly CTW mode 1 coastal SLA within the 10–20 day period (Figure 12a), while in the SEA it impacts a broader frequency band ranging from submonthly to intraseasonal time scales (Figure 12b).

Hence, our results suggest that subseasonal wind stress forcing can account for the increase in the amplitude of the first CTW mode south of 25°S (15°S) in the SEP (SEA). It explains the loss of coherence between the coastal variability and the equatorial forcing at ∼30°S in the SEP. In addition to the dissipation and scattering of the remotely forced CTW mode 2 in the SEA, subseasonal wind stress forcing also participates in the early decreasing of the equatorial teleconnection in the SEA.

4. Conclusions and Discussion

In this paper, we have investigated the subseasonal poleward coastal propagations in the southeastern Pacific and Atlantic Oceans. The main objective is to explain the 15° difference between the two systems in the maximum latitude at which the coastal variability remains consistent with the equatorial forcing, as observed from altimetry. Our methodology is based on the experimentation with a combination of regional ocean general circulation model simulations and simple linear CTW model simulations, for which twin configurations of the SEP and SEA coastal oceans have been developed. We first quantified the amplitude of the subseasonal oceanic forcing in both eastern equatorial basins in terms of eastward-propagating EKW. Results show that this forcing is only 20% larger in the Pacific than in the Atlantic. However, we reported important differences in the relative contribution of the different baroclinic modes: the first EKW mode dominates the EEP variability, while in the EEA, EKW mode 2 carries a greater fraction of the subseasonal energy. Then, a decomposition of ROMS model outputs into CTW contribution was performed following the methodology validated in the companion paper (Illig et al., 2018). In both systems, the extracted CTW modes propagate at velocities close to the theoretical phase speeds (companion paper Illig et al., 2018). Notably, they propagate slightly faster in the Atlantic compared to the Pacific. This is due to the CTW structures being more barotropic in the SEA than in the Humboldt Current system, which is a consequence of the gentler and shallower topography slope encountered in the SEA. Our study shows that, in both systems, the linear CTW dynamics explains a great amount of the coastal SSLA and SASCA variability, consistently with the good agreement between the linear model and ROMS outputs highlighted in the companion paper (Illig et al., 2018). The summed-up contribution of the first four CTW modes accounts for ∼50–90% of the SASCA and SSLA coastal variabilities. In agreement with the equatorial forcing, in the SEP, the first CTW mode largely dominates the coastal subseasonal variability. The assumption of retaining only the first CTW mode characteristics is thus valid in the SEP, in agreement with Brink (1982). In this context, coastal altimetric products or tide gauge measurements can be useful to monitor subseasonal CTW propagations. In the SEA, the second CTW mode is dominant north of 13°S, whereas poleward of 13°S, the first CTW mode is the most energetic. Note that Polo et al. (2008) estimated coastal propagation velocities along the coast of West Africa within 1.5–2.1 m s^{-1} range, consistent with first and second CTW mode phase speeds. The transition between the two modes corresponds to the latitude where the connection between coastal and equatorial variabilities fades out in the SEA (Goubanova et al., 2013; Polo et al., 2008; Figure 1b). We identified three processes that contribute to explain this result. The damping of CTW mode 2 at ∼13°S in the SEA is induced by the frictional dissipation. South of 13°S, the reenergization of the first CTW mode is triggered by frictional modal scattering and subseasonal alongshore wind stress forcing. In the SEP, the less dissipative remotely forced first CTW mode remains energetic at high latitudes. A smaller impact of the equatorial teleconnection is however reported along the southern Chilean coast (Belmadani et al., 2012; Illig et al., 2014; Shaffer et al., 1997). It is attributed to the local wind forcing contribution that becomes more important south of 25°S, where it overshadows the equatorial signal, in agreement with the result from Hormazabal et al. (2001).

In the SEA, we reported an alternation of the dominant CTW mode contributions, with the equatorially forced second CTW mode being the most energetic equatorward of 13°S, while poleward of this latitude the first CTW mode is the dominant contribution to the coastal subseasonal variability. We attributed this change to the bottom friction which dissipates and scatters the second CTW mode. This allows for the propagation of the remotely forced first CTW mode further south which is reenergized by the coastal wind variability south of 15°S. Surprisingly, we did not detect any drastic changes in the CTW characteristics, in terms of bottom friction dissipation or modal coupling, around the ABFZ (∼17°S, not shown). This could be linked to the fact that we consider ROMS stratification at 400 km offshore in the SEA which might differ from the stratification on the shelf. Nevertheless, ROMS stratification remains fairly constant in the 400 km coastal band in both systems (not shown). Instead, our results suggest that the changes in CTW structure and parameters associated with the coastal vertical stratification modification across the ABFZ are compensated by the deepening and steepening of the bathymetry off the Angolan coast between 13°S and 18°S (Figure 5). We further estimated scattering coefficients due to the changes in the shape of CTW eigenfunctions from one latitude to another, as introduced by Johnson (1991). Indeed, when CTW encounter irregularities on the bottom shelf topography or changes in the coastal stratification along their propagation, energy can be transferred between modes. The values of the scattering coefficients estimated along the West African coast reveal that the changes in the vertical stratification associated with the presence of the ABFZ do not trigger significant modal scattering (not shown). In contrast, the passage over the Walvis Ridge (∼19°S–21°S) and the steepening of the bathymetry off Angola coast are associated with a clear increase in scattering coefficients (not shown). This most likely contributes to the fading of the equatorial connection around 12°S. More thorough analyses are required to properly conclude on this specific point. In particular, it would be relevant to further quantify the effect of the changes in the bathymetry and stratification along the wave propagation. This would imply increasing the complexity of the LCM model by adding the modal scattering associated with the changes in the shape of CTW structure from one latitude to another as implemented by Jordi et al. (2005).

In both systems, we reported a distinct contribution of the second CTW mode (more prominent in the SEA) in the northern part of the domains close to the equatorial band, whereas further south there is a dominance of the first CTW mode. Following the same assumption and using the outputs from similar ROMS experiment, Illig et al. (2014) suggested that a CTW mode alternation could explain the drastic increase in poleward coastal propagation velocity observed in the SSLA off Southern Peru (∼18°S, cf., dashed line in Figure 1a). However, we showed in this paper that the contrast between the first and the second CTW modes is weakly marked in the SEP and the 20% contribution of the second CTW mode fades out north of 10°S, which rules out this supposition. We then hypothesized that the CTW acceleration can be triggered by the synoptic submonthly variability of the coastal jet along the coast of Chile. The latter would force CTW simultaneously over an extended coastal region, creating an apparent acceleration of free coastal propagations. But again, the analysis of the ROMS sensitivity experiment in which climatological surface wind stress forcing is prescribed ($ROMS^{EQ}_{SEP}$) depicts the acceleration of the coastal propagations in the Southern Humboldt region (not shown), in agreement with Illig et al. (2014, their Figure 3). This excludes the role of coastal winds in the increase of the CTW velocity. In the light of the results presented in this paper, we conclude that the acceleration of the coastal propagations is likely associated with the change in the nature of the CTW passing from baroclinic vertical structures along the coast of Peru to fast, nearly barotropic waves south of 20°S (Figure 5), as depicted in LCM (Figure 5 of the companion paper (Illig et al., 2018)) and ROMS modal decomposition (Figure 8 of the companion paper (Illig et al., 2018)) outputs.

Finally, this study emphasizes the importance of the vertical structure variability of the remote equatorial dynamics in the eastern equatorial Pacific and Atlantic Oceans. A first baroclinic EKW transmitted along the southwestern coasts of South American and African continents as a fast weakly dissipative first CTW will propagate farther south than higher-order modes. Hence, the characteristics of the remote equatorial forcing can modulate the maximum latitude at which the equatorial dynamics imprints the coastal variability. In this context, Dewitte et al. (2008) showed that the intraseasonal EKW activity undergoes a significant modulation along the equatorial waveguide. Likewise, at interannual time scales, Dewitte et al. (1999, 2003) reported a different contribution for the dominant EKW modes in the EEP, with the dominance of the second and third baroclinic modes. Similar behavior can be anticipated for the EEA forcing, accounting for the strong low-frequency modulation of the oceanic variability in the Tropical Atlantic (Xichen et al., 2016). As a

consequence, the results presented in this study are valid for the 2000–2008 period and for subseasonal frequencies. Further analysis is required for the investigation of the characteristics of equatorial connection at different time scales, such as the interannual variability. Similarly, the strength of the equatorial connection will be affected by the low-frequency modulation of the equatorial dynamics, which can call into question our results for past or future periods.

Acknowledgments
We thank the CNES (OSTST project EBUS-SOUTH) for financial support. Marie-Lou Bachèlery received funding from the EU FP7/2007–2013 under grant agreement 603521 and the NRF SARCHI chair on modeling ocean atmosphere land interactions. The authors thank Boris Dewitte for the valuable discussions throughout the course of this study. We sincerely acknowledge our native (English) scientist Ross Blamey, who kindly helped us improve our French literary writing. We are also grateful to Kenneth H. Brink and Stephen Van Gorder for sharing their programs and kindly answered some technical questions. The authors acknowledge use of the Ferret program (NOAA PMEL, http://ferret.pmel.noaa.gov) for analysis and graphics in this paper. ROMS model and ROMS_TOOLS software can be downloaded from https://www.croco-ocean.org. The ROMS model grid, forcing, and initial conditions were built using the ROMS_TOOLS package (Penven et al., 2008) version 3.1. Computations were performed using facilities provided by the University of Cape Town's ICTS High-Performance Computing team (http://hpc.uct.ac.za). QuikSCAT wind stress data, AVISO Altimetric data, SODA, and ERA-INTERIM reanalysis outputs are freely available to the public on the dedicated websites of these programs. We thank the anonymous reviewers for their comments and suggestions that helped improved the manuscripts.

References

Aman, A., Testut, L., Woodworth, P., Aarup, T., & Dixon, D. (2007). Seasonal sea level variability in the Gulf of Guinea from altimetry and tide gauge. *Revue Ivoirienne des Sciences et Technologie*, *9*, 105–118.

Bachèlery, M.-L., Illig, S., & Dadou, I. (2016a). Interannual variability in the South-East Atlantic Ocean, focusing on the Benguela Upwelling System: Remote versus local forcing. *Journal of Geophysical Research: Oceans*, *121*, 284–310. https://doi.org/10.1002/2015JC011168

Bachèlery, M.-L., Illig, S., & Dadou, I. (2016b). Forcings of nutrient, oxygen, and primary production interannual variability in the southeast Atlantic Ocean. *Geophysical Research Letters*, *43*, 8617–8625. https://doi.org/10.1002/2016GL070288

Bakun, A., & Nelson, C. S. (1991). The seasonal cycle of wind stress curl in subtropical eastern boundary current regions. *Journal of Physical Oceanography*, *21*, 1815–1834.

Belmadani, A., Echevin, V., Dewitte, B., & Colas, F. (2012). Equatorially forced intraseasonal propagations along the Peru-Chile coast and their relation with the nearshore eddy activity in 1992–2000: A modeling study. *Journal of Geophysical Research: Oceans*, *117*, C04025. https://doi.org/10.1029/2011JC007848

Blanke, B., Speich, S., Bentamy, A., Roy, C., & Sow, B. (2005). Modeling the structure and variability of the southern Benguela upwelling using QuikSCAT wind forcing. *Journal of Geophysical Research*, *110*, C07018. https://doi.org/10.1029/2004JC002529

Brink, K. H. (1982). A comparison of long Coastal Trapped Wave theory with observations off Peru. *Journal of Physical Oceanography*, *12*, 897–913.

Brink, K. H. (1987). Coastal ocean physical processes. *Reviews of Geophysics*, *25*, 204–216. https://doi.org/10.1029/RG025i002p00204

Brink, K. H. (1989). Energy conservation in coastal-trapped wave calculations. *Journal of Physical Oceanography*, *19*, 1011–1016.

Brink, K. H. (1991). Coastal trapped waves and wind-driven currents over continental shelf. *Annual Review of Fluid Mechanics*, *23*, 389–412.

Brink, K. H., & Chapman, D. C. (1987). *Programs for computing properties of coastal-trapped waves and wind-driven motions over the continental shelf and slope* (Tech. Rep. WHOI-87-24, 122 pp.). Woods Hole, MA: Woods Hole Institution.

Cane, M. A., & Sarachik, E. S. (1979). Forced baroclinic ocean motions. III: The linear equatorial basin case. *Journal of Marine Research*, *37*, 355–398.

Carr, M.-E. (2002). Estimation of potential productivity in Eastern Boundary Currents using remote sensing. *Deep Sea Research Part II: Topical Studies in Oceanography*, *49*, 59–80.

Carr, M.-E., & Kearns, E. (2003). Production regimes in four eastern boundary current systems. *Deep-Sea Research Part II: Topical Studies in Oceanography*, *50*(22–26), 3199–3221.

Carton, J. A., & Giese, B. S. (2008). A reanalysis of ocean climate using simple ocean data assimilation (SODA). *Monthly Weather Review*, *136*, 2999–3017. https://doi.org/10.1175/2007MWR1978.1

Chaigneau, A., Eldin, G., & Dewitte, B. (2009). Eddy activity in the four major upwelling systems from altimetry (1992–2007). *Progress in Oceanography*, *83*, 117–123.

Chavez, F. P., & Messié, M. (2009). A comparison of eastern boundary upwelling ecosystems. *Progress in Oceanography*, *83*, 80–96.

Chelton, D., Schlax, M., & Samelson, R. (2011). Global observations of nonlinear mesoscale eddies. *Progress in Oceanography*, *91*, 167–216.

Clarke, A., & Ahmed, R. (1999). Dynamics of remotely forced intraseasonal oscillations off the western coast of South America. *Journal of Physical Oceanography*, *29*, 240–258.

Clarke, A. J. (1983). The reflection of equatorial waves from oceanic boundaries. *Journal of Physical Oceanography*, *13*, 1193–1207.

Clarke, A. J., & Shi, C. (1991). Critical frequencies at ocean boundaries. *Journal of Geophysical Research*, *96*, 10731–10738. https://doi.org/10.1029/91JC00933

Clarke, A. J., & Van Gorder, S. (1986). A method for estimating wind-driven frictional, time-dependent, stratified shelf and slope water flow. *Journal of Physical Oceanography*, *16*(6), 1013–1028.

Correa-Ramirez, M. A., Hormazabal, S. E., & Yuras, G. (2007). Mesoscale eddies and high chlorophyll concentrations off Central Chile (29°–39°S). *Geophysical Research Letters*, *34*, L12604. https://doi.org/10.1029/2007GL029541

Cravatte, S., Picaut, J., & Eldin, G. (2003). Second and first baroclinic Kelvin modes in the equatorial Pacific at intraseasonal timescales. *Journal of Geophysical Research*, *108*(C8), 3266. https://doi.org/10.1029/2002JC001511

Dee, D. P., Uppala, S. M., Simmons, A. J., Berrisford, P., Poli, P., Kobayashi, S., et al. (2011). The ERA-Interim reanalysis: Configuration and performance of the data assimilation system. *Quarterly Journal of the Royal Meteorological Society*, *137*, 553–597. https://doi.org/10.1002/qj.828

Dewitte, B., Illig, S., Parent, L., Du Penhoat, Y., Gourdeau, L., & Verron, J. (2003). Tropical Pacific baroclinic mode contribution and associated long waves for the 1994–1999 period from an assimilation experiment with altimetric data. *Journal of Geophysical Research*, *108*(C4), 3121. https://doi.org/10.1029/2002JC001362

Dewitte, B., Illig, S., Renault, L., Goubanova, K., Takahashi, K., Gushchina, D., et al. (2011). Modes of covariability between sea surface temperature and wind stress intraseasonal anomalies along the coast of Peru from satellite observations (2000–2008). *Journal of Geophysical Research*, *116*, C04028. https://doi.org/10.1029/2010JC006495

Dewitte, B., Purca, S., Illig, S., Renault, L., & Giese, B. (2008). Low frequency modulation of the intraseasonal Equatorial Kelvin Wave activity in the Pacific Ocean from SODA: 1958–2001. *Journal of Climate*, *21*, 6060–6069.

Dewitte, B., Reverdin, G., & Maes, C. (1999). Vertical structure of an OGCM simulation of the tropical Pacific Ocean in 1985–1994. *Journal of Physical Oceanography*, *30*, 1562–1581.

Duchon, C. (1979). Lanczos filtering in one and two dimensions. *Journal of Applied Meteorology*, *18*, 1016–1022.

Echevin, V., Aurelie, A., Marina, L., Michelle, G., Olivier, A., Alice, P., et al. (2014). Intraseasonal variability of nearshore productivity in the Northern Humboldt Current system: The role of coastal trapped waves. *Continental Shelf Research*, *73*(2014), 14–30.

Enfield, D. B., Cornejo-Rodriguez, M. D P., Smith, R. L., & Newberger, P. A. (1987). The equatorial source of propagating variability along the Peru coast during the 1982–1983 El Niño. *Journal of Geophysical Research*, *92*, 14335–14346.

Gomez, F., Spitz, Y. H., Batchelder, H. P., & Correa-Ramirez, M. A. (2017). Intraseasonal patterns in coastal plankton biomass off central Chile derived from satellite observations and a biochemical model. *Journal of Marine Systems*, *174* (2017), 106–118. https://doi.org/10.1016/j.jmarsys.2017.05.003

Gonzalez, C. E., Escribano, R., & Hidalgo, P. (2015). Intra-seasonal variation of upwelling and its effects on copepod community structure off central/southern Chile (2002–2009). *Hydrology*, *758*(1), 61–74.

Goubanova, K., Illig, S., Machu, E., Garçon, V., & Dewitte, B. (2013). SST subseasonal variability in the Benguela upwelling system as inferred from satellite observations (2000–2008). *Journal of Geophysical Research: Oceans*, *118*, 2169–9291. https://doi.org/10.1002/jgrc.20287

Grodsky, S. A., & Carton, J. A. (2006). Influence of the tropics on the climate of the South Atlantic. *Geophysical Research Letters*, *33*, L06719. https://doi.org/10.1029/2005GL025153

Gruber, N., Lachkar, Z., Frenzel, H., Marchesiello, P., Münnich, M., McWilliams, J. C., et al. (2011). Eddy-induced reduction of biological production in Eastern Boundary Upwelling Systems. *Nature Geoscience*, *4*(11), 787–792.

Hagen, E., Feistel, R., Agenbag, J., & Ohde, T. (2001). Seasonal and interannual changes in Intense Benguela Upwelling (1982–1999). *Oceanologica Acta*, *24*(6), 557–568. https://doi.org/10.1016/S0399-1784(01)01173-2

Hayashi, Y. (1982). Space-time spectral analysis and its applications to atmospheric waves. *Journal of the Meteorological Society of Japan*, *60*, 156–171.

Hormazabal, S., Shaffer, G., Letelier, J., & Ulloa, O. (2001). Local and remote forcing of sea surface temperature in the coastal upwelling system off Chile. *Journal of Geophysical Research*, *106*, 16657–16671.

Hormazabal, S., Shaffer, G., & Pizarro, O. (2002). Tropical Pacific control of intraseasonal oscillations off Chile by way of oceanic and atmospheric pathways. *Geophysical Research Letters*, *29*(6), 1081. https://doi.org/10.1029/2001GL013481

Huthnance, J. M. (1978). On coastal trapped waves: Analysis and numerical calculation by inverse iteration. *Journal of Physical Oceanography*, *8* (1), 74–92.

Illig, S., Cadier, E., Bachèlery, M.-L., & Kersalé, M. (2018). Subseasonal coastal-trapped wave propagations in the southeastern Pacific and Atlantic Oceans: 1. A new approach to estimate wave amplitude. *Journal of Geophysical Research: Oceans*, *123*, 3915–3941. https://doi.org/10.1029/2017JC013539

Illig, S., & Dewitte, B. (2006). Local coupled equatorial variability versus remote ENSO forcing in an intermediate coupled model of the tropical Atlantic. *Journal of Climate*, *19*(20), 5227–5252.

Illig, S., Dewitte, B., Ayoub, N., Du Penhoat, Y., Reverdin, G., De Mey, P., et al. (2004). Interannual long equatorial waves in the tropical Atlantic from a high-resolution ocean general circulation model experiment in 1981–2000. *Journal of Geophysical Research*, *109*, C02022. https://doi.org/10.1029/2003JC001771

Illig, S., Dewitte, B., Goubanova, K., Cambon, G., Boucharel, J., Monetti, F., et al. (2014). Forcing mechanisms of intraseasonal SST variability off Central Peru in 2000–2008. *Journal of Geophysical Research: Oceans*, *119*, 3548–3573. https://doi.org/10.1002/2013JC009779

Illig, S., Gushchina, D., Dewitte, B., Ayoub, N., & Du Penhoat, Y. (2006). The 1996 equatorial Atlantic warm event: Origin and mechanisms. *Geophysical Research Letters*, *33*, L09701. https://doi.org/10.1029/2005GL025632

Imbol Koungue, R. A., Illig, S., & Rouault, M. (2017). Role of interannual Kelvin wave propagations in the equatorial Atlantic on the Angola Benguela current system. *Journal of Geophysical Research: Oceans*, *122*, 4685–4703. https://doi.org/10.1002/2016JC012463

Jacobs, G. A., Hurlburt, H. E., Kindle, J. C., Metzger, E. J., Mitchell, J. L., Teague, W. J., et al. (1994). Decade-scale trans-Pacific propagation and warming effects of an El Niño anomaly. *Nature*, *370*, 360–363.

Johnson, E. R. (1991). The scattering at low frequencies of coastally trapped waves. *Journal of Physical Oceanography*, *21*, 913–932.

Jordi, A., Orfila, A., Basterretxea, G., & Tintoré, J. (2005). Coastal trapped waves in the Northwestern Mediterranean. *Continental Shelf Research*, *25*, 185–196.

Junker, T., Mohrholz, V., Siegfried, L., & van der Plas, A. (2017). Seasonal to interannual variability of water mass characteristics and currents on the Namibian shelf. *Journal of Marine Systems*, *165*, 36–46. https://doi.org/10.1016/j.jmarsys.2016.09.003

Kessler, W. S., McPhaden, M. J., & Weickmann, K. M. (1995). Forcing of intraseasonal Kelvin waves in the equatorial Pacific. *Journal of Geophysical Research*, *100*, 10613–10631. https://doi.org/10.1029/95JC00382

Kondo, J. (1975). Air-sea bulk transfer coefficients in diabatic conditions. *Boundary-Layer Meteorology*, *9*, 91–112.

Leth, O. (2000). *Ocean circulation in the eastern South Pacific: An observational and numerical modelling study* (PhD thesis, 184 pp.). Copenhagen, Denmark: Niels Bohr Institute, University of Copenhagen.

Mahadevan, A. (2014). Eddy effects on ocean biogeochemistry. *Nature, News and Views*, January 2014. https://doi.org/10.1038/nature13048

Marchesiello, P., & Estrade, P. (2007). Eddy activity and mixing in upwelling systems: A comparative study of northwest Africa and California regions. *International Journal of Earth Sciences*, *98*, 299–308. https://doi.org/10.1007/s00531-007-0235-6

Meyers, S. D., Melsom, A., Mitchum, G. T., & O'Brien, J. (1998). Detection of the fast Kelvin wave teleconnection due to El Nino-Southern Oscillation. *Journal of Geophysical Research*, *103*, 27655–27663.

Moore, D. W. (1968). *Planetary-gravity waves in an equatorial ocean* (PhD thesis). Cambridge, MA: Harvard University.

Morrow, R., Birol, F., Griffin, D., & Sudre, J. (2004). Divergent pathways of cyclonic and anti-cyclonic ocean eddies. *Geophysical Research Letters*, *31*, L24311. https://doi.org/10.1029/2004GL020974

Narayan, N., Paul, Mulitza, A., & Schulz, S. M. (2010). Trends in coastal upwelling intensity during the late 20th century. *Ocean Science*, *6*, 815–823.

Penven, P., Echevin, V., Pasapera, J., Colas, F., & Tam, J. (2005). Average circulation, seasonal cycle, and mesoscale dynamics of the Peru Current System: A modeling approach. *Journal of Geophysical Research*, *110*, C10021. https://doi.org/10.1029/2005JC002945

Penven, P., Marchesiello, P., Debreu, L., & Lefevre, J. (2008). Software tools for pre- and post-processing of oceanic regional simulations. *Environmental Modelling & Software*, *23*, 660–662.

Picaut, J. (1983). Propagation of the seasonal upwelling in the eastern equatorial Atlantic. *Journal of Physical Oceanography*, *13*, 18–37.

Pietri, A., Testor, P., Echevin, V., Chaigneau, A., Mortier, L., Eldin, G., et al. (2013). Finescale vertical structure of the upwelling system off Southern Peru as observed from glider data. *Journal of Physical Oceanography*, *43*, 631–646. https://doi.org/10.1175/JPO-D-12-035.1

Pizarro, O., Clarke, A. J., & Van Gorder, S. (2001). El Niño sea level and currents along the South American Coast: Comparison of observations with theory. *Journal of Physical Oceanography*, *31*(7), 1891–1903. https://doi.org/10.1175/1520-0485(2001)031<1891:ENOSLA>2.0.CO;2

Pizarro, O., Shaffer, G., Dewitte, B., & Ramos, M. (2002). Dynamics of seasonal and interannual variability of the Peru-Chile Undercurrent. *Geophysical Research Letters*, *29*(12), 1581. https://doi.org/10.1029/2002GL014790

Polo, I., Lazar, A., Rodriguez-Fonseca, B., & Arnault, S. (2008). Oceanic Kelvin waves and tropical Atlantic intraseasonal variability: 1. Kelvin wave characterization. *Journal of Geophysical Research*, *113*, C07009. https://doi.org/10.1029/2007JC004495

Regime shifts in demersal assemblages of the Benguela Current Large Marine Ecosystem: A comparative assessment (PDF download available). Retrieved from https://www.researchgate.net/publication/271909566_Regime_shifts_in_demersal_assemblages_of_the_Benguela_Current_Large_Marine_Ecosystem_A_comparative_assessment

Rouault, M., Illig, S., Bartholomae, C., Reason, C. J. C., & Bentamy, A. (2007). Propagation and origin of warm anomalies in the Angola Benguela upwelling system in 2001. *Journal of Marine Systems*, *68*(3–4), 473–488. https://doi.org/10.1016/j.jmarsys.2006.11.010

Rouault, M., Illig, S., Lübbecke, J., & Imbol Koungue, R. A. (2018). Origin, development and demise of the 2010–2011 Benguela Niño. *Journal of Marine Systems.* Retrieved from https://www.sciencedirect.com/science/article/pii/S0924796316303876; https://doi.org/10.1016/j.jmarsys.2017.07.007

Schumann, E. H., & Brink, K. H. (1990). Coastal-trapped waves off the coast of South Africa: Generation, propagation and current structures. *Journal of Physical Oceanography*, *20*, 1206–1218.

Sciremammano, F. (1979). A suggestion for the presentation of correlations and their significance levels. *Journal of Physical Oceanography*, *9*, 1273–1276.

Shaffer, G., Pizarro, O., Djurfeldt, L., Salinas, S., & Rutllant, J. (1997). Circulation and low-frequency variability near the Chilean coast: Remotely forced fluctuations during the 1991–1992 El Niño. *Journal of Physical Oceanography*, *27*, 217–235.

Shaffer, G., Hormazabal, S., Pizarro, O., & Salinas, S. (1999). Seasonal an dinterannual variability of currents and temperature off central Chile. *Journal of Geophysical Research*, *104*, 29951–29961.

Shannon, L. V., & O'Toole, M. J. (2003). Sustainability of the Benguela: Ex Africa semper aliquid novi. In G. Hempel & K. Sherman (Eds.), *Large marine ecosystems of the world—Trends in exploitation, protection and research* (pp. 227–253). Amsterdam, the Netherlands: Elsevier.

Shchepetkin, A. F., & McWilliams, J. C. (2005). The Regional Oceanic Modeling System: A split-explicit, free-surface, topography following-coordinate ocean model. *Ocean Modelling*, *9*, 347–404. https://doi.org/10.1016/j.ocemod.2004.08.002

Stramma, L., Bange, H. W., Czeschel, R., Lorenzo, A., & Frank, M. (2013). On the role of mesoscale eddies for the biological productivity and biogeochemistry in the eastern tropical Pacific Ocean off Peru. *Biogeosciences*, *10*, 7293–7306. https://doi.org/10.5194/bg-10-7293-2013

Tim, N., Zorita, E., & Hünicke, B. (2015). Decadal variability and trends of the Benguela upwelling system as simulated in a high-resolution ocean simulation. *Ocean Science*, *11*, 483–502. https://doi.org/10.5194/os-11-483-2015

Tomczak, M., & Godfrey, J. S. (1994). *Regional oceanography: An introduction* (422 pp.). New York, NY: Pergamon.

van der Lingen, C. D., Shannon, L. J., Cury, P., Kreiner, A., Moloney, C. L., Roux, J. P., et al. (2006). Resource and ecosystem variability, including regime shifts, in the Benguela Current System. In V. Shannon et al. (Eds.). *Benguela: Predicting a large marine ecosystem* (pp. 147–185). Amsterdam, the Netherlands: Elsevier.

Vega, A., Du Penhoat, Y., Dewitte, B., & Pizarro, O. (2003). Equatorial forcing of interannual Rossby waves in the eastern South Pacific. *Geophysical Research Letters*, *30*(5), 1197. https://doi.org/10.1029/2002GL015886

Xichen, L., Xie, S.-P., Gille, S., & Yoo, C. (2016). Atlantic-induced pan-tropical climate change over the past three decades. *Nature Climate Change*, *6*, 275–279.